



# Numerical modeling of hydraulic control, solitary waves and primary instabilities in the Strait of Gibraltar

Margaux Hilt, Laurent Roblou, Cyril Nguyen, Patrick Marchesiello, Florian Lemarié, Swen Jullien, Franck Dumas, Laurent Debreu, Xavier Capet, Lucie Bordoïs, et al.

## ► To cite this version:

Margaux Hilt, Laurent Roblou, Cyril Nguyen, Patrick Marchesiello, Florian Lemarié, et al.. Numerical modeling of hydraulic control, solitary waves and primary instabilities in the Strait of Gibraltar. *Ocean Modelling*, 2020, 155, pp.101642. 10.1016/j.ocemod.2020.101642 . hal-02418114

**HAL Id: hal-02418114**

**<https://inria.hal.science/hal-02418114>**

Submitted on 6 Jan 2021

**HAL** is a multi-disciplinary open access archive for the deposit and dissemination of scientific research documents, whether they are published or not. The documents may come from teaching and research institutions in France or abroad, or from public or private research centers.

L'archive ouverte pluridisciplinaire **HAL**, est destinée au dépôt et à la diffusion de documents scientifiques de niveau recherche, publiés ou non, émanant des établissements d'enseignement et de recherche français ou étrangers, des laboratoires publics ou privés.

# Numerical Modeling of Hydraulic Control, Solitary Waves and Primary Instabilities in the Strait of Gibraltar

M. Hilt<sup>a,\*</sup>

*14 avenue Edouard Belin, 31400 Toulouse, France*

*L. Roblou<sup>a</sup>, C. Nguyen<sup>a</sup>, P. Marchesiello<sup>b</sup>, F. Lemarié<sup>d</sup>, S. Jullien<sup>c</sup>, F. Dumas<sup>f</sup>, L. Debreu<sup>d</sup>, X. Capet<sup>g</sup>, L. Bordois<sup>f</sup>, R. Benshila<sup>c</sup>, F. Auclair<sup>a</sup>*

*<sup>a</sup>Laboratoire d'Aérodynamique, Université de Toulouse, CNRS, UPS, France*

*<sup>b</sup>LEGOS/IRD, 31400 Toulouse, France*

*<sup>c</sup>LEGOS/CNRS, 31400 Toulouse, France*

*<sup>d</sup>Univ Grenoble Alpes, Inria, CNRS, Grenoble INP, LJK, Grenoble, France*

*<sup>e</sup>Ifremer, Univ. Brest, CNRS, IRD, Laboratoire d'Océanographie Physique et Spatiale (LOPS), IUEM, F- 29280, Plouzané, France*

*<sup>f</sup>Service Hydrographie et Océanographie de la Marine, Brest, France*

*<sup>g</sup>LOCEAN/IPSL, CNRS/UPMC/IRD/MNHN, Paris, France*

---

## Abstract

A two-dimensional, vertical section of the Strait of Gibraltar is simulated numerically with the nonhydrostatic / non-Boussinesq three-dimensional CROCO model to investigate details of small-scale dynamics. The proposed configuration is simple, computationally efficient and incorporates the configuration of sills characteristic of this region. Despite the shortcomings of a 2D representation, this configuration provides a realistic depiction of small-scale mechanisms in the strait during a typical tidal cycle: internal solitary waves generation and propagation, occurrence of hydraulic controls and hydraulic jumps at the sills and presence of active turbulent patches. In particular, the well-known eastward propagation of large amplitude internal waves is assessed using the Korteweg de Vries (KdV) propagation model for solitary waves.

As a step towards establishing a realistic three-dimensional Large Eddy Simulation (LES), the sensitivity of the configuration to various choices (e.g., resolution, amplitude of tidal forcing or numerical schemes) is investigated. Our analyses indicate that the representation of small-scale dynamics in the Strait of Gibraltar can be much improved by increasing resolution and relaxing the hydrostatic assumption. Further studies are necessary to grasp the mechanisms of mixing and/or stirring induced by this fine scale processes.

**Keywords:** Strait of Gibraltar, Internal Solitary Waves, nonhydrostatic

---

\*Corresponding author

Email address: [margaux.hilt@aero.obs-mip.fr](mailto:margaux.hilt@aero.obs-mip.fr) (M. Hilt)

## 1. Introduction

[Figure 1 about here.]

The Strait of Gibraltar connects two major basins : the Northern Atlantic and the Mediterranean Sea, over which evaporation exceeds precipitation and river run-off. To compensate the resulting loss, exchanges of mass and salt are required through the strait. Figure D.1 illustrates the rather complex exchanges occurring there. Inflowing Atlantic water is less salty (salinity  $S_A \approx 36$ ) than the outflowing Mediterranean water ( $S_M > 38$ ), and spreads as a surface layer in the Alboran Sea. The interface between the two water masses is distorted by undulations that are not precisely periodic with regard to the tidal cycle but exhibit regularity in some areas. One of the paper objectives is to better understand the small-scale processes that lead to the Atlantic and Mediterranean water masses transformation in the vicinity of the Strait of Gibraltar.

To further illustrate the exchange between the Northern Atlantic and the Mediterranean, a very simple steady-state model can be expressed as a system of two basic conservation equations.

Volume conservation is expressed as :

$$Q_A + Q_M = E - P \quad (1)$$

while the conservation of salt requires:

$$Q_A S_A + Q_M S_M = 0 \quad (2)$$

where  $Q_A$  is the Atlantic water volume flux (positive),  $Q_M$  is the Mediterranean water volume flux (negative), both localized in the Strait of Gibraltar, and  $E - P$  is the space-averaged Evaporation minus Precipitation (and river runoff) water budget integrated over the whole Mediterranean Sea.  $E - P$  is positive.  $S_A$  ( $S_M$ ) stands for Atlantic (Mediterranean) water mean salinity and  $S_M - S_A \approx 2$  (Bethoux, 1979). The water budget  $E - P$  is positive in the Mediterranean due to excess evaporation that correspond to a yearly averaged loss of water of about 1 meter over the whole basin (Garrett et al., 1990).

A major dynamical feature in the Strait of Gibraltar is the so-called "flow criticality" usually characterized by the Froude number ( $F$ ): it compares the internal wave phase speed with a flow characteristic velocity. Several definitions of the non-dimensional Froude number can be found in the literature: it can notably be defined for each layer, resulting in a composite number for the whole water column, as in Farmer and Armi (1988) or in Sannino et al. (2009b).

A "subcritical" (respectively "supercritical") regime lies in the range of small (respectively large) values of the Froude number  $F < 1$  (respectively  $F > 1$ ), with an intermediate "critical" regime for  $F \approx 1$ . The upstream propagation of internal waves is inhibited for supercritical flow so that a hydraulic control

occurs at the transition from subcritical to supercritical flow; it persists during periods and within regions of large Froude numbers. As such, the hydraulic regime at a given point will vary in time according to substantial currents variations occurring along the tidal cycle. It is, for example, well established that large amplitude solitary waves in the Strait of Gibraltar can develop due to the hydraulic control at Camarinal Sill (Farmer and Armi, 1988), making it a crucial process to represent.

Several analytical models have been proposed to investigate the hydraulic control in the Gibraltar region (Bryden and Stommel, 1984; Farmer and Armi, 1986; Garrett et al., 1990). The hydraulic control usually occurs in these models at Camarinal Sill (CS), Espartel Sill (ES), and Tarifa Narrows (TN), although the modelled hydraulic control location and frequency vary according to the model refinement :

1. Farmer and Armi (1986)'s two-layer model accounts for the strait geometry (depth and width), the exchanged volumes ( $Q_A$  and  $Q_M$ ) and the salinity contrast ( $S_A - S_M$ ). This simple model is able to simulate two hydraulic controls: the first one located by the sill, the other in the TN contraction, defining "maximal exchange regime" (further details are given below).
2. In a slightly more elaborated model, the inclusion of entrainment between the two layers and the subsequent interfacial layer introduction modify the left-hand terms of equations (1) and (2) with the introduction of horizontal and vertical transports in the interfacial layer (Bray et al., 1995). Critical conditions are changed within such two interfaces model which may support two baroclinic modes and new hydraulic controls (Sannino et al., 2009b).
3. Considering a three-dimensional flow, the definition of the control needs to account for cross-strait variations such as the tilt of the density interface in the latitudinal direction. In the maximal exchange solution, control in TN may induce the detachment of the surface layer from the northern coast (Sannino et al., 2009b).

The hydraulic control effect within the strait is illustrated in Figure D.1. The flow is initially subcritical in the Strait; the propagation of internal waves is not hindered at the interface between Atlantic and Mediterranean waters (denoted "a" in Figure D.1); then the tidal flood in the vicinity of the Camarinal Sill becomes supercritical. In the supercritical to subcritical transition, downstream of the sill, a "hydraulic jump" ("b" in Figure D.1) may occur.

Hydraulic jumps are large-amplitude depressions in the regions where hydraulic controls occur. There, intense mixing between the Atlantic and Mediterranean waters takes place as observed by Wesson and Gregg (1994). Shear flow instabilities can develop in the hydraulic jump of the Camarinal Sill (denoted "c" in Figure D.1).

The release of hydraulic jumps generates large-amplitude, non-linear, non-hydrostatic Internal Solitary Waves (ISW) trains (denoted "d" in Figure D.1) (Farmer and Armi, 1988). As the barotropic tide is constrained by the bathymetry,

81 large vertical velocities appear and induce energy transfer to several normal  
 82 modes of internal waves. Some observations in the Strait of Gibraltar identify  
 83 the largest ISW amplitude to the first baroclinic mode ; for which vertical ve-  
 84 locities have the same direction throughout the water column and all isopycnal  
 85 surface displacements are in phase. The signature of Mode 2 waves (the verti-  
 86 cal velocity profile exhibits one node) has also been observed in the region of  
 87 Gibraltar strait (Farmer and Armi, 1988; Vázquez et al., 2006). The internal  
 88 waves propagate at the interface of Mediterranean and Atlantic waters.

89 As the strait flow varies at various timescales during the year, some devia-  
 90 tion is expected in the occurrence of the hydraulic control in the strait. This  
 91 may have a wide impact since local flow conditions combined with the above  
 92 two conservation equations (1 and 2) determine the relation between the vol-  
 93 ume fluxes, the evaporation minus precipitation budget ( $E - P$ ) and the salinity  
 94 difference ( $S_A - S_M$ ) (Bryden and Kinder, 1991). Practically, an "overmixed"  
 95 solution corresponds to a minimal salinity difference and a maximal exchange of  
 96 water mass in the strait : it would thus constrict the formation of Mediterranean  
 97 waters and diapycnal mixing over the Mediterranean basin (Bryden and Stom-  
 98 mel, 1984; Garrett et al., 1990). Moreover, the small-scale processes occurring  
 99 in the strait itself can directly modify the local characteristics of Mediterranean  
 100 waters (García-Lafuente et al., 2011; Naranjo et al., 2015) and Atlantic waters  
 101 (Millot, 2014). This can affect their characteristics as they enter respectively in  
 102 the North Atlantic sub-basin and in the Mediterranean Sea.

103 To study the flow dynamics in the strait in further details, more realistic  
 104 numerical modelling is of great help. Early attempts used two-layer models  
 105 (Brandt et al., 1996; Izquierdo et al., 2001). The increase of computational  
 106 power led to 3D modelling (Sannino et al., 2004) with increasing vertical and  
 107 horizontal resolution, explicitly addressing the tidal cycle and flow characteris-  
 108 tics. More recently, even nonhydrostatic models have been used (Sánchez Gar-  
 109 rido et al., 2011; Sannino et al., 2014) to explicitly represent the ISW. Other  
 110 configurations include the Strait of Gibraltar into a Mediterranean circulation  
 111 model (Soto-Navarro et al., 2015). In this case, the increased resolution lo-  
 112 cally in the strait (Naranjo et al., 2014) — or the nesting of high-resolution  
 113 grids within a coarse resolved regional model (Sannino et al., 2009a) — shows  
 114 a clear impact on Mediterranean stratification and improves the representation  
 115 of convective events in the northwestern Mediterranean basin.

116 The coastal and regional ocean modelling community model (CROCO<sup>1</sup>) is  
 117 based on a new nonhydrostatic and non-Boussinesq solver (Auclair et al., 2018)  
 118 developed within the former ROMS kernel (Shchepetkin and McWilliams, 2005),  
 119 for an optimal accuracy and cost efficiency. CROCO opens up new perspec-  
 120 tives in terms of modelling of small-scale processes (Fox-Kemper et al., 2019;  
 121 Lemarié et al., 2019). In this sense, the present study objectives are also nu-  
 122 merical: we show that a new generation of nonhydrostatic ocean models can be  
 123 used efficiently to simulate complex nonlinear, fine scale physics in a realistic

---

<sup>1</sup><http://www.croco-ocean.org/>

124 but computationally-affordable configuration. The complete solution of Navier-  
125 Stokes equations are thus solved numerically for the very first time in a complex  
126 realistic regional configuration.

127 The present configuration of the Strait of Gibraltar is based on a classi-  
128 cal lock-exchange initialization (Sannino et al., 2002). A 2D vertical section of  
129 the strait is adopted in order to reduce the number of parameters impacting  
130 the studied dynamics. This rather simple configuration is thus of weak com-  
131 putational cost and reduces the implementation burden; it allows to reach the  
132 horizontal and vertical scales of the largest turbulent structures observed in this  
133 area. In the strait, where most transverse dynamical feature are an order of  
134 magnitude weaker, our numerical approach is some kind of ersatz of a large-  
135 eddy simulation (LES<sup>2</sup>), for which at least the generation process of primary  
136 instabilities is correctly represented. However, LES is a 3D concept as the route  
137 to molecular dissipation differs in 2D and 3D turbulence. The present study is  
138 focused on the description of the largest primary instabilities in the Strait of  
139 Gibraltar ; as well as providing order of magnitudes for explicit simulations of  
140 these dynamics. Along with these physical aims, the relevance of the chosen  
141 numerical methods is a major concern. A quantified impact of the largest tur-  
142 bulent structures on the water masses is out of the scope of what is presented  
143 hereafter: it would require a fully three dimensional LES ( also achievable with  
144 the CROCO model ), in complement with dedicated relevant experimental mea-  
145 surements.

146 In Section 2, we present an overview of CROCO equations and the implemen-  
147 tation for the 2D lock-exchange experiment. We describe the implementation  
148 of the bathymetry profile, water masses, and the exchange and tidal flows. In  
149 Section 3, we analyse the physics of the 2D configuration, comparing the model  
150 solution to already published data (e.g., in Farmer and Armi (1988)). Emphasis  
151 is then made on the hydraulic control (Section 3.2), the hydraulic jump (Sec-  
152 tion 3.3) and the mode-1 and mode-2 ISW (non-linear internal trains of solitary  
153 waves) propagation (Section 3.4). Last, the sensitivity to the tidal forcing am-  
154 plitude and to the numerical choices are analysed respectively in sections 4.1  
155 and 4.2, with a focus on the fine-scales dynamics listed in Figure D.1.

## 156 2. Model Description and Configuration

### 157 2.1. The Numerical Modeling System

158 The proposed numerical model of the Strait of Gibraltar simulates explicitly  
159 the fine-scale processes (from tens to hundreds of meters) discussed previously.  
160 This assumes that (i) a sufficient grid resolution is provided in the strait and  
161 (ii) a well-suited numerical kernel is used.

---

<sup>2</sup>LES (Large Eddy Simulation): LES, as opposed to DNS (Direct Numerical Simulation) does not cope with the full 3D Kolmogorov energy cascade down to molecular scales. However at least the onset of this cascade (the largest turbulent structures) is explicitly represented, unlike in RANS (Reynolds Averaged Navier-Stokes).

162 The nonhydrostatic (non-Boussinesq) CROCO version is chosen for its abil-  
 163 ity to allow the explicit representation of primary instabilities that cascade the  
 164 kinetic energy injected at large scale down to the smaller scales. This direct  
 165 transfer ends at the finest scale resolved; the subgrid dissipation of energy is  
 166 performed both by the implicit mixing of the advection schemes and the ex-  
 167 plicit closure schemes. The dissipation is solely performed by (quasi-)monotonic  
 168 numerical advection schemes (Grinstein et al., 2007) when no parametrized tur-  
 169 bulent closure scheme accounts for the sugrid-scale mixing.

170 CROCO is an extension of ROMS from which it inherited the robustness  
 171 and efficiency of its time-splitting implementation, the accuracy of high-order  
 172 methods, including its pressure gradient scheme for terrain-following coordi-  
 173 nates, and computing performances (Shchepetkin and McWilliams, 2005; De-  
 174 breu et al., 2012; Soufflet et al., 2016). In CROCO's time-splitting algorithm,  
 175 the "slow mode" is similar to ROMS internal (baroclinic) mode (Shchepetkin  
 176 and McWilliams, 2005); its "fast mode" includes the usual external (barotropic)  
 177 mode and a new pseudo-acoustic mode that allows computation of the nonhy-  
 178 drostatic pressure within a non-Boussinesq formalism (Auclair et al., 2018). A  
 179 two-level time-splitting kernel is thus conserved in CROCO (as opposed to the  
 180 first implementation of the 3-level time-splitting by Auclair et al. (2018)) but the  
 181 fast time step integrates a 3D-compressible flow. Furthermore the slow internal  
 182 mode is enhanced by a prognostic equation of the vertical velocity, replacing  
 183 the hydrostatic equation.

## 184 2.2. Continuous, Free-Surface, Compressible Equations

185 The full set of Navier-Stokes equations for a free-surface ocean is explic-  
 186 itly integrated, including the continuity and momentum equations, the surface  
 187 kinematic relation, the heat, salt and state equations in Cartesian coordinates :

$$\partial_t \rho = -\vec{\nabla} \cdot (\rho \vec{v}) \quad (3)$$

$$\partial_t \rho \vec{v} = -\vec{\nabla} \cdot (\rho \vec{v} \otimes \vec{v}) - 2\rho \vec{\Omega} \wedge \vec{v} - \vec{\nabla} p + \rho \vec{g} + \mu \Delta \vec{v} + \lambda \vec{\nabla} (\vec{\nabla} \cdot \vec{v}) \quad (4)$$

$$\partial_t \zeta = w(z=\zeta) - \vec{v}(z=\zeta) \cdot \vec{\nabla} \zeta \quad (5)$$

$$\partial_t \rho \theta = -\vec{\nabla} \cdot (\rho \theta \vec{v}) + \kappa_\theta \Delta \theta \quad (6)$$

$$\partial_t \rho S = -\vec{\nabla} \cdot (\rho S \vec{v}) + \kappa_S \Delta S \quad (7)$$

$$\rho = \varrho(\theta, S, P) \quad (8)$$

188 where  $\vec{v} = (u, v, w)$  is the velocity,  $p$  the total pressure,  $\zeta$  the free-surface  
 189 anomaly,  $\rho$  the density,  $\theta$  and  $S$  the potential temperature and salinity re-  
 190 spectively.  $\vec{\Omega}$  is the instantaneous earth rotation vector,  $\vec{g}$  is the acceleration of  
 191 gravity and  $\mu$ ,  $\lambda$ ,  $\kappa_\theta$  and  $\kappa_S$  are respectively the dynamical and second (bulk)  
 192 viscosity and the thermal and salinity diffusivities.  $\varrho(\theta, S, P)$  is a linear approx-  
 193 imation of the seawater equation of state.

### 2.3. Density and Pressure Decomposition

As part of the time-splitting, the density is splitted into one slow and one fast component based on a first-order decomposition with respect to the total pressure. In the following,  $s$  and  $f$  subscripts refer to these slow and fast components respectively.

$$\rho = \rho_s(\theta, S, P) + \overbrace{\left. \frac{\partial \rho}{\partial P} \right|_{\theta, S}}^{\delta \rho = \rho_f} \delta P + O(\delta P^2) \quad (9)$$

$$P = \underbrace{P_{atm} + \int_z^\zeta (\rho_s - \rho_0) g \, dz'}_{\text{Slow mode}} + \underbrace{\rho_0 g(\zeta - z) + \underbrace{\delta P}_{P_f}}_{\text{Fast mode}} \quad (10)$$

No further decomposition is required for the other variables. Note that  $\delta P$  is the nonhydrostatic pressure.

### 2.4. Slow vs Fast Components

Navier-Stokes equations are integrated with two different time-steps in a time-splitting algorithm. The slow mode is identical to ROMS whereas the fast mode is now 3D and includes the integration of the compressible terms of the momentum and continuity equations. The free-surface anomaly is computed through the surface kinematic condition.

$$\begin{aligned} \partial_t \rho_f &= -\partial_t \rho_s - \vec{\nabla} \cdot (\rho \vec{v}) \\ \partial_t \rho \vec{v} &= \overbrace{-\vec{\nabla} \cdot (\rho \vec{v} \otimes \vec{v}) - 2\rho \vec{\Omega} \wedge \vec{v} - \vec{\nabla} \left( \int_z^{\zeta_f} (\rho_s - \rho_0) g \, dz' \right) + \mu \Delta \vec{v}}^{\vec{\Lambda}_s} \\ &\quad \underbrace{-\rho_0 g \vec{\nabla} \zeta_f - \vec{\nabla} P + \rho \vec{g} + \lambda \vec{\nabla} (\vec{\nabla} \cdot \vec{v})}_{\vec{\Lambda}_f} \quad (11) \\ \partial_t \zeta_f &= w_f(z=\zeta) - \vec{v}_f(z=\zeta) \cdot \vec{\nabla} \zeta_f \\ \partial_t \rho \theta_s &= \Theta_s = -\vec{\nabla} \cdot (\rho \theta_s \vec{v}) + \kappa_\theta \Delta \theta_s \\ \partial_t \rho S_s &= \Sigma_s = -\vec{\nabla} \cdot (\rho S_s \vec{v}) + \kappa_S \Delta S_s \\ \rho_s &= \varrho(\theta_s, S_s, \zeta_f) \\ \rho_f &= c_s^{-2} P_f \end{aligned}$$

The momentum equations are integrated both in the slow and fast modes but the right-hand-side of the equation is split in two parts: a "slow" part ( $\vec{\Lambda}_s$ )

made of slowly varying terms (advection, Coriolis force, baroclinic pressure force and viscous dissipation) and a "fast" part ( $\vec{\Lambda}_f$ ), made of fast-varying terms (the surface-induced and compressible pressure force, the weight and dissipation associated with bulk-viscosity). This momentum equation is numerically integrated twice, once with a large time-step keeping  $\vec{\Lambda}_f$  constant, and once with a smaller time-step keeping  $\vec{\Lambda}_s$  constant. This time-splitting is much more computationally efficient than integrating the whole set of equations at the same short time step.

The general, compressible equations set 11 can basically propagate three types of waves: internal and external gravity waves, and acoustic waves propagating at  $c_s$ , the speed of sound. The nonhydrostatic pressure anomaly is not a solution of a diagnostic elliptic Poisson-like equation as it is for a Boussinesq equations set. The pressure anomalies travel at the acoustic waves velocity. The acoustic solver is not global anymore (as it is in the Poisson-like set); it is now local in space, meaning that no 3D global linear system of equations needs to be inverted anymore. The price of solving fast acoustic waves is however enhanced due to a more restrictive CFL conditions. Both acoustic and surface waves are integrated in CROCO's fast mode with a smaller time-step to cope with this. As a linear set of simplified compressible equations needs to be integrated in this fast mode the whole computations remain affordable. In addition, since the sound speed is at least one order of magnitude larger than the phase-velocity of the fastest propagating waves and much larger than any ocean advection velocity, it can be artificially reduced. The only requirement is that the speed of sound remains larger than any other propagating wave or flow velocity in the domain. In particular, it must remain larger than the phase-velocity of long surface waves so that nonhydrostatic anomalies can be propagated vertically fast enough to set up the corresponding wave structure over the water column. Sensitivity tests show that, in this case, a slower sound speed has no impact on lower-frequency dynamics in the region of the strait: more details on that point can be found in Auclair et al. (2018).

## 2.5. Bathymetry

[Figure 2 about here.]

Figure D.2.a presents the 500-m-resolution bathymetry gathered in the framework of the HOMONIM project coordinated by the French Navy (SHOM) and MétéoFrance, and as provided by the French Navy (Biscara et al., 2016). The main bathymetric features as well as the localization of the studied 2D vertical section are exhibited. This section is chosen as close as possible to the transect of Farmer and Armi's Gibraltar Experiment performed in April 1986 (Farmer and Armi, 1988) and coincides in the western area with the Mediterranean waters privileged path. Hereafter,  $u$  is the velocity in the longitudinal direction of the section and  $v$  the velocity in the transverse direction. Figure D.2.b presents the Gibraltar Strait width according to different reference depths. This plot shows that an averaged thirteen kilometer width can be used, featuring steep slopes at the lateral boundaries of the strait, especially in Tarifa Narrows.

Simulations are performed with 50m and 220m horizontal resolutions. The bathymetry used in the simulations is averaged laterally to limit the unrealistic effect of local seamounts in the transverse direction such as those found in TN (which can end up acting as another sill in a 2D vertical section). To that end, a Gaussian interpolation of the bathymetry along the section in Figure D.2.a is used with a greater Gaussian radius in the transverse direction than in the longitudinal direction. The Gaussian radius in the transverse direction is set to 1500 m (i.e. lower than the width of the strait in figure D.2.b). As a consequence, the bathymetry only reflects the deepest areas in the canal. In the longitudinal direction, the Gaussian interpolation radius is set to 300 m to preserve the bathymetry variability in this direction.

The minimum depth thus assessed at Camarinal Sill (i.e. the main sill in the Strait), along the transect's path goes from the value of approximately 200 m to 245 m. The model bathymetry used is the one shown in Figure D.1. A reference simulation (hereafter named **SimRef**) is carried out at 50-m horizontal resolution with additional characteristics and parameters listed in D.1.

[Table 1 about here.]

[Figure 3 about here.]

## 2.6. Initial Water Masses, Tidal Forcing and Boundary Conditions

The temperature and salinity reference profiles are chosen to initialise the density field of the simulations. A minimum of two profiles for each of those variables is needed to initialize gradients associated with sloping isopycnal surfaces in a given direction. According to Sannino et al. (2002), a lock-exchange initialization is performed with homogeneous Atlantic water initially to the west of the CS and homogeneous Mediterranean water to the east. A three-day spin-up described in Section 2.7) is then performed to set up the exchange flow in the strait.

The initial temperature and salinity profiles are presented in Figure D.3. The contrast in salinity between Atlantic and Mediterranean waters is noticeable, with respective mean values of 35.9 and 38.2.

In the following, the interface between Atlantic and Mediterranean layers is taken as the 37 isohaline, following Bryden et al. (1994). Density is now expressed as an anomaly (written  $\rho'$ ) relative to a reference (mean) density  $\rho_0$ . From now on, the implicit reference density (unless contraindicated) will be  $\rho_0 = 1033.7 \text{ kg/m}^3$ : a value reached in the pycnocline separating the two water masses.

An idealized M2 tidal forcing (of period  $T = 12.4 \text{ h}$ ) is prescribed at the open boundaries after the spin-up period (at  $t = 3 \text{ days} = 5.8 T$ ). It is introduced thanks to a barotropic current of amplitude 0.4 m/s at the western boundary (0.8 m/s at CS), corresponding to a moderate regime according to the TPXO-8 tidal atlas (Egbert and Erofeeva, 2002). Lateral forcing is introduced at the open eastern and western boundaries through mixed active passive radiation

conditions (Marchesiello et al., 2001) ; cyclic conditions are imposed to the northern and southern open boundaries.

## 2.7. Initial Flow and Effect of Coriolis Force

The Gibraltar strait lateral boundaries are distant of about 15 km, with a clear funneling effect from the CS to the eastern end of the strait (  $5.4^\circ\text{W}$ ; see Figure D.2.b). The internal Rossby radius  $R$  (Appendix A) is usually found to vary from 10 to 20 km (Bormans and Garrett, 1989; Candela et al., 1990; Vlasenko et al., 2009). The width of the strait and the Rossby radius  $R$  being of the same order of magnitude, rotational effects can be neglected as a rather good approximation. Therefore, the momentum balance is mainly between the acceleration and the pressure force in the equation (4) and the geostrophic adjustment in the along-strait direction is locally neglected. In their observations (Farmer and Armi, 1988) and the 3D-modeling configurations (Sannino et al., 2002), the consequence of Earth’s rotation is a cross-strait shear of along-strait velocity (Bormans and Garrett, 1989) and a tilt of the isopycnals: along the southern boundary (i.e. along the Moroccan coast), the interfacial isopycnal is deeper and the flow reaches larger velocities.

As the transverse flow, the coastal boundaries, and the resulting “funneling effect” cannot be simulated in a 2D vertical section, it is necessary to examine whether completely ignoring rotational effects is viable in a 2D vertical approximation. To that end, three different numerical simulations of the stratification and the mean circulation are compared: (i) one simulation with the Coriolis force activated from start to end (**SimAllCor**;  $f = 8.5 \cdot 10^{-5} \text{s}^{-1}$ ), (ii) the second one without the Coriolis force (**SimNoCor**;  $f = 0$ ), and (iii) the last one with the Coriolis force activated only after a three days spin-up period (**SimRef**). Apart from the Coriolis parameter, all the three simulations were performed with the characteristics given in Table D.1 for **SimRef**. During the very first hours of simulation time, the ‘Lock-Exchange dam’ separating the Atlantic and Mediterranean water-masses disappears; a gravity current is generated with dense Mediterranean waters flowing down the western slope of CS and light Atlantic water spreading in the surface layer east of the sill.

Figure D.4 presents the field of the longitudinal velocity ( $u$ ) as well as some isopycnals for **SimAllCor** (a) and **SimNoCor** (b) at  $t = 72 \text{ h}$  (i.e., the end of the spinup period). The bold isopycnal surface  $\rho' = -0.7 \text{ kg/m}^3$  corresponds at that time to the 37psu-isohaline. Figures D.4.a-b also present the transverse-velocity ( $v$ ) isotachs  $\pm 0.5 \text{ m/s}$ . Figures D.4.c-d show the tidal residual components  $u$  and  $v$  in the water column at the two dashed vertical lines on figures D.4.a-b. These locations correspond to the moorings indicated in Figure 1 of Candela et al. (1990). Using the 37psu-isohaline as a frontier between the two water masses, the 3T time-averaged transport through the left dashed line at the CS is given in the columns labelled ‘Transport’ of the Table D.2.

In **SimNoCor** (Figure D.4.b), a clear vertical shear of the along-section velocity can be seen between the two water masses. The shear is still featured in the 3T-averaged current profiles of Figure D.4.c and is, for station M2, in accordance with the observations given by the moorings at the CS. This shear has

342 decreased since initialization as progressive mixing of the two water masses re-  
 343 duces the baroclinicity. The currents in **SimAllCor** and **SimRef** are weaker,  
 344 with locally negative currents in the upper layer (see Figure D.4.c). This is  
 345 confirmed by the layer-averaged transports presented in Table D.2, where val-  
 346 ues in **SimAllCor** and **SimRef** are one order of magnitude smaller than in  
 347 **SimNoCor**. Using an average strait's width of 13 km, an approximate baro-  
 348 clinic transport for the strait can be estimated from the values in Table D.2;  
 349 for **SimNoCor** it would be of 0.6 Sv: it is slightly weaker than the range of  
 350 0.7-1 Sv estimated from various field observations (see a review in Sammartino  
 351 et al. (2015)). In **SimAllCor** and **SimRef**, the cross-section velocity is due to  
 352 the inclusion of the Coriolis force. More precisely, during the spin-up phase of  
 353 **SimAllCor**, the effect of rotation can no more be neglected after 6 hours. At  
 354 that time, the upper Atlantic layer has spread over a distance of about 26 km  
 355 and the cross-section velocity featured in Figure D.4.a is already significant.

356 [Figure 4 about here.]

357 With no coastal boundaries to hinder the geostrophic adjustment within the  
 358 strait, the initially longitudinal gravity current is almost completely converted  
 359 into transverse geostrophic current with spurious (non physical) consequences  
 360 on the slope of the isopycnals. Geostrophy enables a thermal-wind balance for  
 361 the transverse  $v$  component:

$$\frac{\partial v}{\partial z} = -\frac{g}{\rho_0 f} \frac{\partial \rho}{\partial x} \quad (12)$$

362 This is particularly apparent to the east of the CS in Figure D.4.a where the  
 363 pycnocline is located at the transition between positive and negative transverse  
 364 velocities. As a consequence, the pycnocline slope is  $\Delta z/\Delta x = 6.10^{-3}$  (Table  
 365 D.2) and the Atlantic water cannot spread further than the resulting surface  
 366 front. In **SimRef**, the Coriolis force is introduced only after a 72-h-spin-up  
 367 period leading to the state presented in Figure D.4.b. In this case, the resulting  
 368 slope and transverse velocity are smaller than in **SimAllCor**. The pycnocline in  
 369 the eastern part of the domain is deeper whereas it is shallower in the western  
 370 part. However, longitudinal currents remain weak. In contrast, in **SimNo-**  
 371 **Cor** the thermal-wind balance is not allowed and, away from the sills,  $\Delta z/\Delta x$   
 372 vanishes. In the longitudinal direction, the main balance is between the pres-  
 373 sure force ( $-1/\rho_0 \partial p/\partial x$ ) and the acceleration term. In this case, the shear of  
 374 the longitudinal velocity is better represented at the two moorings. The larger  
 375 transports in both layers indicate that a larger amount of Mediterranean water  
 376 enters the Tangier basin than in **SimAllCor**. This is confirmed by the strati-  
 377 fication (Figure D.4.a and Table D.2) since the pycnocline is shallower over the  
 378 Espartel Sill (and deeper within the TN).

379 A perfect balance between the transports in the upper and lower layers is  
 380 not achieved in any of these three numerical experiments. While there is no  
 381 numerical challenge in achieving longer simulation, the fluxes of Mediterranean  
 382 and Atlantic waters are not realistically specified to re-stratify properly the

water column in these academic configurations. After the spin-up period, the intense tidal mixing and other dissipative processes may end up homogenizing the initial water masses. The gap between the transports in the upper and lower layers disappears as the depth-averaged absolute transports decrease. This process is faster in **SimNoCor** than in the other configurations in which the thermal-wind balance maintains the isopycnal slopes. In this case, the depth of the 37 psu-isohaline, taken as a moving average over one tidal period at  $x = 5.4^\circ\text{W}$ , increases from 130 to 175 m in **SimNoCor** over three tidal periods (not shown). This impacts the large-amplitude internal waves propagation.

The difficulty to obtain both realistic ambient stratification and circulation is a limitation of the restriction to a 2D vertical section of the dynamical problem targeted. In the proposed implementation, an initial state is obtained by lock-exchange with a spin-up period of 72 h dedicated to the adjustment of the gravity current produced by the 'dam break'. For the remainder of this paper, the reference simulation (**SimRef**) is chosen as the simulation whose adjustment is made in a non-rotating framework. This initial state has a correct mean exchange but it is weakened as the tidal forcing is introduced and changes the stratification conditions.

To mitigate this problem, the rotation is restored at the end of the spin-up period: the geostrophic balance that ensues stabilizes the slopes of isopycnals by generating a transverse current. The mean exchange is nevertheless reduced but the stratification (i.e. both the slope of the isopycnals and the vertical density gradient) thus saved is crucial to the generation and propagation of the large-amplitude solitary waves. Furthermore, the small-scale processes discussed hereafter take place during the tidal cycle. At this time-scale, the barotropic exchange is dominated by the tidal currents, so that in the reference simulation, the amplitude of the baroclinic exchange is correct. Note that if rotation is activated from the beginning of the spin-up period (**SimAllCor**), it leads to unrealistically-large slopes of the isopycnals (see Table D.2).

### 3. The Reference Simulation

The reference simulation presented previously is now evaluated thanks to the observational data from the Gibraltar Experiment (Farmer and Armi, 1988). We describe the hydraulic controls, the primary instabilities and the dynamics of the ISW in this reference simulation.

#### 3.1. Comparison with in situ Observations

In the present section, observations from the Gibraltar Experiment (Farmer and Armi, 1988) are investigated in order to evaluate the quality of the model solution obtained with the reference configuration **SimRef**.

The table D.2 presents the pycnocline depth and slope at different locations along the section for the three configurations and the observational data. The depth and slope for **SimAllCor** and **SimNoCor** are calculated after 72 h of simulation and correspond to the isopycnal surface  $\rho' = -0.7 \text{ kg/m}^3$  in figures D.4.a-b, whereas for configuration **SimRef** the same isopycnal taken in

426 a 3T-averaged stratification corresponding to Figure D.5. In **SimAllCor**, the  
 427 isopycnals have a greater slope than the reported observations from Gibraltar  
 428 Experiment (0.006 vs 0.003). In **SimNoCor**, there is no slope away from the  
 429 sills, while as discussed before, the slope obtained in **SimRef** is small. The  
 430 stratification in **SimRef** is close to that of **SimNoCor** in the eastern part  
 431 with an isopycnal close to the horizontal. In the western part and over the CS,  
 432 the pycnocline is shallower than in the other two simulations (Table D.2).

433 In the following, we further investigate small-scale dynamical processes such  
 434 as hydraulic jump and ISW propagation in configuration **SimRef**. This is  
 435 also the baseline configuration used to perform all sensitivity tests presented  
 436 hereafter.

437 [Table 2 about here.]

### 438 3.2. Tidal Currents & Hydraulic Control.

439 [Figure 5 about here.]

440 In the present study, the Froude number ( $F$ ) is simply defined at each grid  
 441 point as the ratio between the local longitudinal velocity  $u$  and the theoretical  
 442 speed  $c_1$  of the first internal wave mode, computed with the modal decomposition  
 443 for each point of the x-axis (see Appendix B for details).

444 For single-layer flows, hydraulic control occurs in the region of transition  
 445 between subcritical and supercritical flows. In this region, the condition  $F > 1$   
 446 is met over the whole water column. For multi-layer flows, the Froude number  
 447 condition may be satisfied in a few layers only. In this case, the layers where  
 448 the flow becomes supercritical are considered as "hydraulically controlled".

449 Three areas of potential hydraulic control in Gibraltar Strait are identified  
 450 from previous studies: the CS, the ES and the narrowest part of the TN (near  
 451  $5.5^\circ\text{W}$  longitude in figure D.2). Farmer and Armi (1988) found persistent con-  
 452 trols for first internal wave mode at the ES, the CS and the TN. Sannino et al.  
 453 (2009b) found only ephemeral appearances of such controls, except at the ES  
 454 where it is permanent. The discrepancy is likely lying in the definition and the  
 455 estimation of the composite Froude number.

456 Figure D.5 shows the regions where the flow is critical. Closed contours  
 457 indicate the locations of critical Froude number ( $F = 1$ ), inside which the flow  
 458 is supercritical. The longitudinal velocity fields ( $u$ ) used to estimate  $F$  are  
 459 taken at maximum outflow (grey) at  $t = 7.5 T$  and maximum inflow (black)  
 460 at  $t = 8 T$ . The internal waves phase speed  $c_1$  is computed from the 3T-  
 461 time-averaged stratification represented in Figure D.5. No control of the first  
 462 mode is ever seen in TN : this is a consequence of the 2D simplification which  
 463 excludes the representation of the tidal flow intensification by the narrowing  
 464 of the strait at TN. On the other hand, hydraulic control is expected at both  
 465 sills. The location where it should occur alternate between the eastern (during  
 466 ebb) and western (during flood) sides of the sills, with a return to subcritical  
 467 flow when tidal current slackens. The Froude number easily goes beyond 2 in  
 468 the Mediterranean outflow at CS, where the flow is supercritical through most

of the water column, except sometime at the surface. At ES, the lower layer may become supercritical with Froude number that never exceeds 1.5. The lack of persistent control at ES may be a consequence of the crudely imposed stratification.

### 3.3. Primary Instabilities in the Hydraulic Jump Area

[Figure 6 about here.]

One manifestation of the hydraulic control is the formation of hydraulic jumps in specific regions where the flow transitions from supercritical to subcritical. This is a complex area with steep slopes and high shears where flow-topography interaction can generate small-scale coherent structures. The largest ones are resolved in **SimRef** and are characterised here with various methods. First, the Okubo-Weiss parameter (Appendix C) is computed to investigate the presence of new 'coherent structures' in the hydraulic jump area. Their dynamics are further investigated using Empirical Orthogonal Functions (EOFs) computed with a Singular Value Decomposition (SVD). Their typical length and velocity scales are finally compared with the expected analytical values of shear instabilities and lee waves.

The dynamics of the CS hydraulic jump are illustrated in Figure D.6, in which the density field (Fig. D.6.a) and the vertical velocity field (Fig. D.6.b) over the western slope of the CS are represented during flood. Several flow parameters were also computed and are depicted in Figure D.6.a and b. These parameters are :

1. The Froude number defined in Appendix B. The contours of critical Froude number  $F = 1$  are shown in Figure D.6.b, inside which the flow is supercritical.
2. The Richardson gradient number defined as  $Ri = N^2 / (\partial u / \partial z)^2$ , with  $N$  the Brunt-Väisälä frequency defined in Eq.13. Contours of  $Ri = 0.25$  are depicted in Figure D.6.a, as  $Ri < 0.25$  is a required condition for the development of shear instabilities.

$$N = \sqrt{-\frac{g}{\rho_0} \frac{\partial \rho}{\partial z}} \quad (13)$$

3. The Okubo-Weiss parameter defined in Appendix C. Negative values of OW indicate vortical circulation, and so contours of  $OW = -4 * 10^{-4} s^{-2}$  are shown in both Figure D.6.a and b.

In Figure D.6.b, the supercritical flow region ( $F > 1$ ) follows the slope of the sill where the velocity in the Mediterranean outflow is larger than 2 m/s (see the contour  $F = 1$  running approximately parallel to isopycnals between  $5.76^\circ W$  and  $5.77^\circ W$ ). At  $5.77^\circ W$ , the density field in Figure D.6.a shows a sharp transition (e.g., isopycnal  $\rho' = -0.5 kg/m^3$  rises from 350 to 225 m depth), and forms a wedge-shaped region over the supercritical Mediterranean outflow. This is the signature of an internal hydraulic jump.

Downstream of the hydraulic jump, several small-scale structures are visible. Figure D.6.a shows patches of lighter water (billows) associated with areas of negative OW values at a depth of 400 m, and large-amplitude disturbances of isopycnals at 150 m. Negative OW values are also located at troughs and can reach  $OW = -4 * 10^{-4} s^{-2}$ . Both types of structures are propagating westward and are quite probably shed from the internal hydraulic jump at the tip of the wedge-shaped region at  $5.773^{\circ}W$ , with the size of billows growing rapidly as they travel down-slope. In the potential generation area, Richardson number values are less than 0.25, indicating favorable conditions for generation of primary shear instabilities.

Further identification of the simulated new features of Figure D.6 is achieved by proceeding with a complex singular value decomposition (SVD) (Pairaud and Auclair, 2005) of the velocity field ( $w+iu$ ) in the water column between  $5.795^{\circ}W$  and  $5.78^{\circ}W$  longitude, during outflow conditions. This region is highlighted in Figure D.7.a, in which the time mean field of longitudinal velocity  $u$  is presented, showing the intense outflow below layers of lesser velocities. The mean density field and location of  $Ri < 0.25$  are also indicated, the former showing a homogeneous area between 50-150 m above the seafloor. The SVD gives a first singular vector responsible for 28 % of the total variance corresponding to the evolution of the barotropic forcing (not shown). The remaining singular eigenvectors have lesser corresponding variance and show smaller structures with high-frequency variations in the singular right eigenvector. Two consecutive singular vectors often have very close eigenvalues and temporal variations.

[Figure 7 about here.]

Figure D.7.b shows the reconstructed field of the combination of the second and third singular vectors (respectively responsible for 13 % and 11 % of total variance) added to the mean field shown in Figure D.7.a. The Okubo-Weiss parameter is again computed for the resulting velocity field, which shows two rows of y-axis vortices centered at  $z = -300$  m (anti clockwise) and  $-400$  m (clockwise). The upper row of vortices appears to generate the observed interface oscillations.

Based on  $OW=0$  contours, the lower clockwise vortices have an estimated horizontal scale of 200 m and a vertical scale of 150 m, corresponding to horizontal and vertical wavenumbers  $3.10^{-2}$  and  $4.10^{-2} m^{-1}$  respectively. Their propagation speed can be estimated as  $-0.7$  m/s by following the center of the billows defined by areas of negative OW values. The distance between the centers of two consecutive vortices is  $L = 530$  m. The centers of the upper anti-clockwise and lower clockwise vortices are shifted along flow by  $L/2$ , so that the extrema of their respective vertical velocities are aligned vertically. It seems that a transfer of momentum occurs between the two rows of vortices in a way reminiscent of the Vallis model of edge waves in a stratified region of a shear flow (pp 254-258 in Vallis (2006)).

The length scales deduced from this SVD analysis can now be compared with expected scales from simple analytical models for shear instabilities and

552 internal waves based on the general characteristics of the flow on the western  
 553 slope of Camarinal.

554 Shear flow instability in a two-layer system of infinite depth results in a mixed  
 555 interface of vertical extent  $\Delta H$  expressed by equation 14.6 of Cushman-Roisin  
 556 and Beckers (2011) :

$$\Delta H \approx \frac{1}{k_{min}} = \frac{\rho_0(u_1 - u_2)^2}{2(\rho_2 - \rho_1)g} \quad (14)$$

557 with  $k_{min}$  the wave-number of the most unstable mode in this system, taken as  
 558 the scale of the primary instability that will develop. In the generation area of  
 559 CS,  $(u_1 - u_2)$  is in the range of 1.2 to 2 m/s and  $(\rho_2 - \rho_1)$  is in the range of  
 560 1.2 to 1.7 kg/m<sup>3</sup>. Additional values are  $\rho_0 = 1033.7$  kg/m<sup>3</sup> and  $g = 9.81$  m<sup>2</sup>/s.  
 561 This gives a range of vertical scales between 44 m and 183 m and  $k_{min}$  between  
 562  $2.10^{-2} \text{ m}^{-1}$  and  $5.10^{-3} \text{ m}^{-1}$ . The scales of the simulated lower row of vortices  
 563 are in the upper part of this range.

564 Lee waves are another candidate for small-scale transient flow and the inter-  
 565 facial oscillations observed in our solutions. Their generation over topography is  
 566 expected when tidal excursion is larger than the topographic length scale  $1/k_b$ ,  
 567 i.e.  $k_b u_0 / \omega > 1$  (St. Laurent and Garrett, 2002). The slopes of Camarinal Sill  
 568 are not symmetrical, as can be seen for example in Figure D.4. On the western  
 569 side of the sill, the depth increases from 250 m (at 5.76°W) to 510 m (at 5.78°W)  
 570 over only 1.8 km, whereas on the eastern side it increases from 250 m to 620 m  
 571 (at 5.65°W) over 9.4 km.  $k_b$  is thus chosen in a range between  $3.10^{-3} \text{ m}^{-1}$  and  
 572  $6.10^{-4} \text{ m}^{-1}$ .  $u_0 = 0.4 \text{ m/s}$  is the amplitude of the barotropic tidal current away  
 573 from the sill. In these conditions, the ratio  $k_b u_0 / \omega$  ranges between 1.7 (over the  
 574 west slope) and 8.9 (over the east slope). Based on this, we cannot rule out the  
 575 possibility that lee waves are generated over the CS.

576 If the simulated small-scale structures would originate from lee waves, their  
 577 phase speed would be comparable to a mode-1 internal gravity waves. This  
 578 can be estimated using the same method as in Appendix B for the average  
 579 stratification presented in Figure D.7.a. It yields a value of 1.4 m/s in the  
 580 area down-flow of the hydraulic jump, which is twice the estimated propagation  
 581 speed of both rows of simulated structures. Therefore, even though lee-wave  
 582 generation is theoretically possible, the interfacial oscillations observed in the  
 583 simulation appear more consistent with the stirring effect of the bottom coherent  
 584 vortices, whose scales fall within the range of expected values for KH instability.

585 We conclude that coherent structures are clearly identified in our simulations.  
 586 They are generated in an area of potentially unstable shear ( $Ri < 0.25$ ) and  
 587 are associated with billows of lighter mixed fluid. The deeper row of vortices  
 588 can reasonably be interpreted as Kelvin-Helmholtz primary instabilities. Their  
 589 downstream behaviour further corresponds to a 2D pairing of two consecutive  
 590 Kelvin-Helmholtz billows. These billows are advected in a region of westward  
 591 flow between the Mediterranean vein and Atlantic waters up until 5.8°W. At this  
 592 location, advection is reduced as the lower layer decelerates and the billows are  
 593 uplifted in a flow recirculation and mixed in the pycnocline. These small-scale  
 594 features appear in the simulation for as long as the hydraulic jump is present,

595 injecting water from the pycnocline in the outflow and vigorously mixing the  
 596 Atlantic and Mediterranean waters until the tidal currents weaken sufficiently  
 597 for the flow to become subcritical.

598 However, the dynamics simulated in a 2D vertical section with no transverse  
 599 flow and no transverse instability may differ from the real ocean. In a fully  
 600 3D configuration, primary Kelvin-Helmholtz instabilities should decay faster as  
 601 secondary Kelvin-Helmholtz instabilities develop along the transverse rotation  
 602 axis of the primary billows. This is precluded in the present 2D configuration,  
 603 even with enhanced resolution, as only y-axis billows can occur.

604 Wesson and Gregg (1994) observed billow structures in the area of CS with  
 605 an extension of several tens of meters. This length scale is much smaller than the  
 606 one simulated in the present numerical configuration. However, these observa-  
 607 tions were made in shallower regions, i.e. probably closer to the generation area:  
 608 larger billows more in line with those simulated in the present study could thus  
 609 develop downstream. Further observations on site are needed, although short  
 610 length-scales and fast propagation speed would require adapted measurement  
 611 strategies.

### 612 3.4. Internal Tide Dynamics

613 [Figure 8 about here.]

614 In **SimRef**, two main types of large amplitude wave propagating eastward  
 615 can be observed. Both of them are generated at CS while tidal currents reverse  
 616 from westward to eastward. This is illustrated in Figure D.8.a-b. First, a mode-  
 617 1 wave appears as a bore over the sill’s crest approximately 2.25 hours after the  
 618 westward flow peaks. In Figure D.8.a, it has propagated over the eastern slope of  
 619 the sill’s crest and is now at 5.7°W longitude: the corresponding profile in Figure  
 620 D.8.c has only one maximum as expected for a mode-1 internal wave. This wave  
 621 rapidly steepens while a hydraulic control is maintained on the western side of  
 622 the sill with lower values of the Froude number. One hour and 15 minutes later,  
 623 the flow becomes subcritical and a large-amplitude mode-2 wave crosses the sill.  
 624 In Figure D.8.b, this new wave is propagating over the eastern slope of the sill;  
 625 its vertical velocity profile is presented in Figure D.8.c. It exhibits two maxima  
 626 of opposite signs and a zero-crossing at the pycnocline’s depth as expected for a  
 627 mode-2 internal wave. Additionally, it can be seen in this figure that the bore-  
 628 like wave has evolved into a train of internal solitary waves, whose propagation  
 629 is discussed below.

630 The propagation of internal waves can be characterized by plotting a space-  
 631 time evolution of a particular isopycnal. In Figure D.9.b, the depth evolution of  
 632 the  $-0.7 \text{ kg/m}^3$  isopycnal is represented (also in a white contour in Fig. D.8).  
 633 Regions of sharp horizontal density gradients can be identified periodically in the  
 634 region of the CS next to 5.76°W longitude. They correspond to the generation  
 635 of hydraulic jumps. The propagation of internal waves are identified by the tilt  
 636 of isolines, whose slopes provide an estimate of wave propagation speed. There  
 637 are differences from one tidal cycle to the next because mixing progressively  
 638 changes the background stratification in the domain. In the following, we focus

on the tidal cycle  $t = 7.5 T - 8.5 T$  (second cycle after the end of the spin-up phase), for which the three-tidal-cycle averaged velocity shear and stratification are shown in Figures D.4 and D.5.

The mode-1 bore of Figure D.8.a propagates down-slope of the CS into the TN, where it experiences a transition into a train of solitary waves moving at a speed of 1.5 m/s. In Figure D.9.c, such a train made of four mode-1 waves can be seen at  $5.5^\circ\text{W}$  longitude. The amplitude of the first wave reaches 100 m. The solitons train amplitude momentarily increases and exceeds 150 m as it propagates over the slope near  $5.5^\circ\text{W}$  longitude in the TN (still during ebb tide). From then on, the wave amplitude decreases as it propagates towards the deeper region. Meanwhile the dispersion increases the number of waves as well as their wavelength as noticed in the space-time diagram which shows the envelop of the train of solitons expanding while it propagates eastward. The dispersion as simulated in CROCO is compared with the Korteweg deVries model in Appendix D.

Similarly, the mode-2 wave shown in Figure D.8.b propagates through the shallowest part of the TN at a speed of 0.9 m/s as a new hydraulic jump is being generated over the eastern slope of CS. It is located at  $5.65^\circ\text{W}$  longitude in Figure D.9.c, with an amplitude of approximately 100 m. The propagation speed of this mode-2 internal wave subsequently decreases when it reaches the deepest part of the domain while simultaneously the tidal phase shifts to flood. The amplitude of these waves is simultaneously strongly reduced.

The signatures of other large-amplitude internal waves can be seen propagating to the west of the CS in Figure D.9.b. They are mode-1 and mode-2 internal waves with amplitude in the tens of meters, i.e. smaller than the eastward propagating wave. They are generated when tidal currents switch from eastward to westward in the same fashion as previously described for the wave train produced east of the CS (as tidal currents reverse from westward to eastward).

As discussed in Section 3.2, a hydraulic control also occurs at the ES. Figure D.9.b shows the same variations of isopycnal depth in this area as near the CS during the tidal cycle  $t \in [7.5 T, 8.5 T]$ , but not on the following cycle anymore. In the latter case, the computed Froude number does not exceed 0.7, as opposed to previous cycles ( $t \in [6.5 T, 7.5 T]$  and  $t \in [7.5 T, 8.5 T]$ ) or later ones ( $t \in [9.5 T, 10.5 T]$  and  $t \in [10.5 T, 11.5 T]$ ). In these cases, the variations are similar and hydraulic control occurs at ES. The sequence is as in CS, with a hydraulic control briefly lost at the barotropic flow reversal. Then internal mode-1 waves of 50-m amplitude at a depth of 300 m are released and propagate toward the CS. In Figure D.9.c, a mode-1 wave can be found at  $5.87^\circ\text{W}$ . These waves dissipate in the area near the sill as the absolute value of the barotropic current decreases.

In Figure D.9.c, two vertical lines are drawn in the TN. They refer to measurements made by Farmer and Armi (1988): the lines indicate the first two baroclinic modes locations three and a half hours after high tide. The right-hand vertical line corresponds to a mode-1 wave and is in agreement with the simulation. However, in **SimRef**, the distance between the two modes is twice

as large as in the observations. Based on observed wave arrivals at various stations, Farmer and Armi (1988) estimated the propagation speed of both mode-1 and mode-2 waves at about 1 to 2.5 m/s for mode 1 and 1 to 1.5 m/s for mode 2. The wave train they observed contained two to three large-amplitude waves, the first one having an amplitude of 100 m. Additional observations by Sánchez Garrido et al. (2008) in the TN region give a propagation speed for mode-1 waves ranging in 1.2 m/s and 2 m/s with a large variation in the velocity of two consecutive wave trains due to the weight of the tidal diurnal inequality (K1 and O1).

The mode-1 dynamics simulated in **SimRef** are consistent with these observations reported by Farmer and Armi (1988) in terms of propagation speed and longitudinal position. However, the simulated mode-2 wave seems too slow and its amplitude too large. Its slower propagation might be due to an underestimation of the barotropic flow that carries the mode-2 within the TN as our 2D vertical approach does not catch well the tunneling effects of this narrowing. This would not affect the mode-1 wave as much, because its linear propagation speed is more intense and the barotropic current advection becomes comparatively small.

The brief hydraulic control loss observed when the tidal currents reverse does not reflect the quasi-permanent control thought to be taking place at ES. In this case, no internal waves packet can be emitted from the ES.

## 4. Sensitivity Testing

The reference configuration presented in the previous section is based on several physical and numerical choices which are now investigated ; mostly the impact of the forcing amplitude, momentum balance (hydrostatic approximation) and numerical parameters (spatial resolution, advection schemes).

### 4.1. Tidal regime

An additional simulation, **SimS**, is first performed similarly to **SimRef** changing only the tidal forcing amplitude. The imposed tidal current amplitude at the western boundary is now increased up to 0.6 m/s, so that it reaches 1.3 m/s over the CS. This corresponds to a spring-tide regime.

Figure D.10 presents a comparison between **SimS** and **SimRef**. In Figure D.10.a, the contours of supercritical regions ( $F > 1$ ) show the the CS hydraulic jump extends further east in **SimS**. As a result, a mode-1 disturbance (denoted "a" in Figure D.10.a) is trapped at  $5.725^\circ\text{W}$  longitude. It propagates eastward when the flow becomes subcritical but the faster bore that is crossing the CS can rapidly catch it up. The outflowing Mediterranean water vein on the westward side of the sill is also thicker in **SimS** and so is the supercritical area. In addition, a new supercritical region appears on the western slope of a secondary relief at  $5.83^\circ\text{W}$  longitude (denoted "b" in Figure D.10.a) with trailing lee waves.

the figure D.10.b shows an eastward propagating mode-1 solitons packet. Since the initial stratifications are similar, linear phase velocities are the same

in **SimRef** and **SimS** at the beginning. The amplitude of the first trough of the train is 50-m larger in **SimS** than in **SimRef**. This should result in increased propagation speed of the solitons in **SimS**, in contradiction with a slower propagation seen in Figure D.10.b. It can be explained by the stronger tidal currents advection in the opposite direction in **SimS**. A mode-2 wave is also generated in both **SimS** and **SimRef**, but is only visible in **SimRef** in Figure D.10.b as it quickly dissipates in **SimS** due to stronger tidal currents. Consistent with our results, Farmer and Armi (1988) show that the ISW amplitude increases with the tidal current during the spring-tide / neap-tide cycle. In addition, two concomitant hydraulic jumps were observed in the strait during spring tide ((Sánchez Garrido et al., 2011)): they exhibit a transverse asymmetry, as the second jump only appears in the northern part of the strait. This could not be confirmed in the present 2D configuration.

[Figure 9 about here.]

#### 4.2. Nonhydrostatic Balance and Numerical Factors

The consequences of several numerical choices are now investigated by running five additional simulations whose differences with **SimRef** are laid out in Table D.3. In particular, the sensitivity to both vertical and horizontal resolution is targeted. A hydrostatic kernel and a WENO5-Z advection scheme for momentum Borges et al. (2008) are also tested and compared with **SimRef**. We focus on the impact of these modifications on two types of small-scale processes studied in the previous sections: the primary (KH) instability generation in the hydraulic jump at the CS, and the eastward propagating solitary waves generated at the same place.

[Table 3 about here.]

##### 4.2.1. Hydraulic Jump and Instabilities

[Figure 10 about here.]

Hydraulic controls (Section 3.2) occur in all simulations, as revealed by systematic estimations of the Froude numbers. Low Richardson numbers ( $< 0.25$ ) are also diagnosed for all simulations over at least part of the CS western slope during flood. However, the features that have been identified as KH instabilities in Section 3.3 do not appear in all simulations. They are absent in the simulations performed in the hydrostatic framework and/or with low horizontal resolution (**SimL**, **SimLH** and **SimH**). Weak horizontal vorticity tilting under the hydrostatic assumption prevents such instabilities to develop. Instead, a smooth, large recirculation appears west of the CS (Figure D.11 for **SimLH**).

In the remaining sensitivity experiments (**SimV** and **SimW**), KH instabilities are generated at the edge of the hydraulic jump and their dynamics is overall similar to the one described in Section 3.3 for **SimRef**: pairing of KH billows can occur whereas anti-clockwise vortices induce oscillations of the interface. Fine resolution (a few tens of meters in the present region) and non-hydrostatic

equations are both required to explicitly simulate the turbulent cascade onset with KH instabilities between Mediterranean and Atlantic flows.

Interestingly enough, a comparison of Figures D.6 (nonhydrostatic configuration) and D.11 (hydrostatic configuration) shows that the fine-scale solution is largely filtered out by the hydrostatic assumption. Without dedicated observations in the area, it remains difficult to conclude that **SimRef** is more realistic, although low Richardson numbers in this region lead us to expect KH instability.

#### 4.2.2. Large Internal Waves

[Figure 11 about here.]

As described in Section 3.4, mode-1 and mode-2 large amplitude internal waves are generated in the CS vicinity and propagate eastward during each ebb in all nonhydrostatic simulations. Figure D.12 presents the density fields in the region of the TN at  $t = 8.1 T$ . A wave train with a minimum of two solitons can only be identified in the nonhydrostatic experiments. In the hydrostatic cases **SimH** and **SimLH**, the lack of nonhydrostatic dispersion produces internal waves propagating as internal bores. In the nonhydrostatic cases, these internal waves can propagate as trains of solitons with varying numbers of solitons (and celerity) : 6 in **SimRef**, 8 in **SimW**, 4 in **SimV**, and 2 in **SimL**.

This illustrates a second aspect of the effect of hydrostatic assumptions, besides the inhibition of turbulent primary instabilities (KH instabilities in the region of the hydraulic jump). As already noted by previous authors (Sannino et al., 2004), the dispersion needed to balance nonlinear steepening in large-amplitude solitary waves is missing in hydrostatic simulations such as **SimH** and **SimLH** (Figure D.12).

#### 4.2.3. Evolution of Stratification

[Figure 12 about here.]

The previous results lead us to anticipate large differences in the way density stratification evolves in **SimRef**, **SimW**, **SimV**, **SimH**, **SimL**, or **SimLH**. To go further, Figure D.13 shows for each configuration the profiles of Brunt-Väisälä frequency ( $N$  defined in eq.13) at  $5.8^\circ\text{W}$  (a) and at  $5.55^\circ\text{W}$  (b). Profiles are time-averaged over one flood.

At  $5.8^\circ\text{W}$ , stratification is similar in **SimH** and **SimLH** with an interface region (defined as the region where  $N$  is maximal, here  $N = 8.10^{-3} \text{ s}^{-1}$ ) located at a depth of 250 m (Figure D.13.a). The nonhydrostatic simulations **SimRef** and **SimL** present an interface region at a similar depth but the vertical gradients are larger in **SimRef** and smaller in **SimL**. **SimV** shows larger vertical gradients of density ( $N = 1.1 \cdot 10^{-2} \text{ s}^{-1}$ ) and a shallower interface at a depth of 150 m. **SimW** is weakly stratified over most of the water column with no clear interface between the two water masses. This result may seem surprising because the WENO5 scheme is of fifth-order accuracy with more selective quasi-monotonic corrections near shocks than the TVD scheme, and is thus expected

810 to produce less smoothing. This apparent contradiction can be explained by the  
811 generation of more intense primary shear instabilities (i.e. with higher values of  
812 associated vertical velocity and vertical velocity gradients), which has the effect  
813 of diffusing density gradients.

814 In Figure D.13.b, averaged  $N$  profiles over one flood are shown at  $5.55^\circ\text{W}$   
815 longitude in a region subjected to intense internal wave activity. **SimH**, **SimLH**  
816 and **SimL** exhibit similar profiles with  $N$  slowly decreasing below the interface  
817 at 160 m. **SimRef** has a similar interface at 160 m but with higher  $N$  value,  
818 although weaker stratification appear at the top of the lower layer. **SimV** and  
819 **SimW** both have shallower interfaces at 130 m, with  $N$  reaching the highest  
820 values in **SimV** ( $N = 1.25 \cdot 10^{-2} \text{ s}^{-1}$ ), as the enhanced vertical resolution allows  
821 the representation of stronger gradients.

822 Clear conclusions cannot yet be drawn concerning mixing. KH instabilities  
823 are expected in the region of the hydraulic jump and downstream. They lead  
824 to more stirring and consequently open up new opportunities to improve mod-  
825 elling of the route to mixing. Further investigation and diagnostics are now  
826 required to better understand the energy cascades. In particular, the present  
827 comparison between WENO5 and TVD advection schemes (and their implicit  
828 dissipation) indicates that numerical choices may unfortunately still have large  
829 consequences. Therefore, the role of physical and numerical closure must be  
830 considered comprehensively (Marchesiello et al., 2011; Soufflet et al., 2016).

## 831 5. Discussion and Conclusion

832 The present study focuses on small-scale dynamics in the Strait of Gibraltar  
833 and on the capacity of a new split-explicit, free-surface, nonhydrostatic regional  
834 oceanic model (CROCO) to represent such dynamics. Both objectives were  
835 pursued in parallel and several seminal results are obtained.

836 The study confirms that the generation of large-amplitude mode-1 and mode-  
837 2 internal waves in the Strait of Gibraltar as well as the onset of stratified  
838 turbulence and its energy cascade can be simulated with a computationally-  
839 efficient 2D vertical section. The characteristics of the simulated internal waves  
840 compare qualitatively well with published observations and previous numerical  
841 studies. Internal tides dynamics and shear instability in the hydraulic jump area  
842 are then analysed in more details, revealing characteristics and mechanisms.

843 The results of the study rely on a new type of nonhydrostatic, non-Boussinesq,  
844 free-surface kernel (Auclair et al., 2018) implemented in the CROCO model. The  
845 resulting compressible oceanic model is presented in a realistic nonhydrostatic  
846 configuration for the first time. Sensitivity tests confirm that a nonhydrostatic  
847 (here non-Boussinesq) kernel is required (i) to simulate ISW trains and (ii) to  
848 explicitly simulate the onset of stratified turbulence energy cascade, provided  
849 that resolution is increased from about 200 m to 50 m. We conclude that reso-  
850 lutions finer than a few hundred meters are required in addition to a refinement  
851 of dynamical equations (relaxation of hydrostatic assumption) in order to solve  
852 the dominant dynamical processes in a key region of the Mediterranean.

Detailed characteristics of the vertical 2D configuration are also given with particular attention to the bathymetry and to the representation of the Coriolis force (implicit representation of funnelling effect in the strait). The proposed approach offers a computationally affordable way to make preliminary investigations of internal-wave dynamics in regions where these waves are important. However, the vertical 2D configuration is limited by the simplified representation of bathymetry and associated biases in the velocity shear between in-flowing Atlantic Waters and out-flowing Mediterranean waters. The inclusion of restratification processes (surface and boundary forcing) would allow the model to remain accurate for a greater number of tidal cycles — the present configuration is considered accurate within three days after the spin-up period, before mixing starts to homogenise the water masses. Several remaining processes could not be considered: the transverse propagation of ISWs in the Strait of Gibraltar (Sánchez Garrido et al., 2011; Vlasenko et al., 2009) and in the Alboran Sea; the hydraulic control at the TN (Farmer and Armi, 1988; Sannino et al., 2009b); the boiling-water over the CS (Bruno et al., 2002) or reflections on the strait’s coasts.

Only the “onset” of turbulence cascade could be simulated showing complex dynamics occurring in the area of the hydraulic jump at CS, with some small scale features identified as primary Kelvin-Helmholtz instabilities. Although this 2D study highlights how interesting this area can be, there is no doubt that simulation of secondary KH instabilities and subsequent energy cascade as well as the long term impact of these small scale processes on Mediterranean and North Atlantic circulation will require a fully 3D LES approach as well as dedicated field campaigns that explore these fine-scale processes.

## Appendix A. Evaluation of the First Internal Rossby Radius

The first internal Rossby radius is defined as :

$$R = \frac{\sqrt{g'h}}{f} \quad (\text{A.1})$$

At the Gibraltar Strait’s latitude, the Coriolis parameter is  $f = 8.5 \times 10^{-5} \text{ s}^{-1}$ . The numerator  $c^* = \sqrt{g'h}$  is the phase speed of the linear interfacial waves, into which the reduced gravity is:

$$g' = g \frac{\rho_M(S_M) - \rho_A(S_A)}{\rho_0} \quad (\text{A.2})$$

where  $\rho_M(S_M) - \rho_A(S_A) \approx 2 \text{ kg/m}^3$ . If the reference density is set to  $\rho_0 = 1033.7 \text{ kg/m}^3$  and the gravity acceleration by  $g = 9.81 \text{ m}^2/\text{s}$ ,  $g' = 0.02 \text{ m/s}^2$  which is in agreement with in situ data (cf Bryden et al. (1994)).  $h$  is a characteristic height given by:

$$h = \frac{h_1 h_2}{h_1 + h_2} \quad (\text{A.3})$$

887 where  $h_1$  and  $h_2$  are respectively the upper and lower layer thicknesses. Picking  
 888 up the data values from Farmer and Armi (1988) (Table D.2, first line), we  
 889 obtain a range of  $h = 50 - 100$  m, which combined with the previous values for  
 890  $g'$  and  $f$  leads to  $R$  ranging in 11.5 km (east of Camarinal Sill) to 16 km (west  
 891 of Camarinal Sill).

892  $\sqrt{g'h}$  can be replaced by the mode-1 internal waves speed( $c_1$ ), which is es-  
 893 timated in the present study (Appendix B) for the 3T-averaged stratification  
 894 (**SimRef**) presented in Figure D.5.  $c_1$  ranges between 0.8 m/s (at Camarinal  
 895 Sill) and 1.8 m/s (in the eastern part of the strait), giving an estimated range  
 896 of Rossby Radius  $c_1/f$  between 9.5 and 21 km for the simulated section.

## 897 Appendix B. Computation of a Froude Number

898 A single value of mode-n linear internal wave phase speed ( $c_n$ ) can be com-  
 899 puted for a flat-bottom and a linear stratification. This velocity can then be  
 900 compared at each depth with the magnitude of local horizontal currents ( $u$ )  
 901 to estimate when and where internal waves can propagate against currents. A  
 902 diagnostic tool is the ratio of velocities, i.e. a Froude number ( $F_n$ ) defined  
 903 as  $F_n = u/c_n$ .  $c_n = \omega/k_n$  where  $\omega$  is the wave frequency, here the M2-tidal  
 904 frequency, and  $k_n$  are eigenvalues obtained by solving numerically the Sturm-  
 905 Liouville problem associated with the linear propagation equation (Gill, 1982):

$$W_n'' + k^2 \frac{N^2 - \omega^2}{\omega^2 - f^2} W_n = 0 \quad (\text{B.1})$$

906 with bottom and surface boundary conditions  $W_n(0) = 0$  and  $W_n(-H) = 0$ .  $W_n$   
 907 gives the structures of vertical modes. For each point on the x-axis, the profile  
 908  $N(z)$  is computed with Eq.13 from the 3T-averaged stratification in **SimRef**  
 909 (shown in Figure D.5).

910 [Figure 13 about here.]

911 The value of the first mode phase speed  $c_1(x)$  is indicated in the lower panel  
 912 of Figure D.14 and compared to the longitudinal velocity  $u(x, z)$  at  $t = 8.5$   $T$   
 913 plotted in the upper panel. The areas where  $u(x, z) > c_1(x)$  (equivalent to  
 914 Froude number  $F_1$  larger than 1) are presented in the upper panel as well. The  
 915 flow inside those contours is called supercritical.

## 916 Appendix C. Computation of Okubo-Weiss Parameter

917 The Okubo-Weiss parameter (OW) is defined as

$$OW = s_n^2 + s_s^2 - \Omega^2 \quad (\text{C.1})$$

918 With  $s_n$  the normal strain component,  $s_s$  the shear strain component and  $\Omega$  the  
 919 vorticity. Usually, it is used in a xy-plane (e.g., for tracking eddies in Chelton

et al. (2007)), but it is computed here in the zx-plane with the strains and vorticity expressed as :

$$s_n = \frac{\partial w}{\partial z} - \frac{\partial u}{\partial x} \quad , \quad s_s = \frac{\partial u}{\partial z} + \frac{\partial w}{\partial x} \quad , \quad \omega = \frac{\partial u}{\partial z} - \frac{\partial w}{\partial x} \quad (\text{C.2})$$

Negative values of OW indicate a greater role of rotation over deformation, and thus the presence of coherent vortices.

#### Appendix D. Comparison with Korteweg-de Vries (KdV) Model

[Figure 14 about here.]

Following many studies (Sánchez Garrido et al., 2008; Sannino et al., 2009b; Vlasenko et al., 2009), the large amplitude internal waves of Section 3.4 are termed "ISWs" for Internal Solitary Waves. To confirm that the internal waves observed in this section are ISWs, they are now compared with solutions of the Korteweg-de Vries equation which is recalled below. The solutions of this equation satisfy a balance between nonhydrostatic dispersion and nonlinear advection. Nonlinear advection steepens the wave front, whereas nonhydrostatic dispersion reduces steepening by transferring energy from large to small scales, resulting in a relatively stable entity called a "solitary" wave, or soliton.

The Korteweg-de Vries (KdV) equation describes the evolution of an infinitely thin interface in a two-layer system with constant bottom topography:

$$\frac{\partial \zeta}{\partial t} + c^* \frac{\partial \zeta}{\partial x} + \underbrace{\frac{3}{2} \frac{h_1 - h_2}{h_1 h_2} c^* \zeta \frac{\partial \zeta}{\partial x}}_A + \underbrace{\frac{1}{6} h_1 h_2 c^* \frac{\partial^3 \zeta}{\partial x^3}}_B - \underbrace{\frac{3}{8} \zeta^2 c^* \frac{h_1^2 + 6h_1 h_2 + h_2^2}{(h_1 h_2)^2}}_C = 0 \quad (\text{D.1})$$

where  $c^*$  is the interfacial speed of small-amplitude internal waves:  $c^* = \sqrt{g'h} = R.f$  and  $\zeta$  is the vertical displacement of the interface.  $g'$  and  $h$  have already been defined in Appendix A. The first two terms on the left-hand-side of (D.1) are those involved in the classical propagation equation for a small-amplitude, linear, interfacial wave travelling in the x-direction at speed  $c^*$ . The third term (bracket A) is a first-order approximation (with respect to amplitude) of nonlinear advection. Term (B) is a dispersive term. The fifth term (C) is a higher-order non-linear term associated with a second order development for advection. The complete equation (D.1) will be referred to as "extended KdV" (or "eKdV"), whereas the same equation without term (C) will simply be referred to as "KdV" (Dossmann, 2012).

The simulated large amplitude waves presented in this study are compared with the solutions of the KdV or eKdV equation to gain insight into their dynamics. For optimal comparison, a new simulation, called **SimRef+** was carried out. Its characteristics are similar to **SimRef** (Table D.1), except that (i) the eastern boundary is shifted 42-km to the east into the Mediterranean sea and (ii) the tidal forcing is stopped after only 7.25 periods. The first eastward-propagating train of mode-1 waves generated by the tide at the CS is compared

955 with the propagation given by numerical integration of the KdV and eKdV  
 956 equations (eq. D.1).

957 The vertical displacement of isopycnal  $\rho' = -0.5 \text{ kg/m}^3$  is extracted<sup>3</sup> at  
 958  $t_0 = 7.5 T$  when the mode-1 ISW train propagates over a region of constant  
 959 depth ( $H = 890 \text{ m}$ ) east of TN (Figure D.15), so as to get closer to the  
 960 KdV framework. The position of the chosen isopycnal surface at this time is  
 961 shown in Figure D.15.a. At that time, the distance between the first and second  
 962 solitons of the train is 5 km; the first soliton has an amplitude of 75 m and the  
 963 train includes 7 solitons. This isopycnal is chosen as initial state for the KdV  
 964 or eKdV model. The KdV and eKdV equations are integrated either with the  
 965 interfacial wave speed ( $c^* \approx 1.27 \text{ m/s}$ ) or with mode-1 velocity ( $c_1 = 1.45 \text{ m/s}$ ;  
 966 see Appendix B for details on  $c_1$  evaluation).

967 Figures D.15.b-e compare the interface depth obtained at  $t = t_0 + 0.25 T$   
 968 in the KdV and eKdV models with the position of the  $-0.5 \text{ kg/m}^3$  isopycnal in  
 969 **SimRef+**. In the latter, the distance between the first two solitons has grown  
 970 since  $t = t_0$  and reaches 7 km with an amplitude of 70 m for the first trough.  
 971 The train is now made of 11 solitons: the first three have decreasing amplitudes,  
 972 then two smaller solitons of comparable amplitude (40 m) and one soliton of  
 973 greater amplitude, followed by solitons with decreasing amplitude again.

974 In the KdV solution obtained with propagation speed  $c^*$  the first solitary  
 975 wave is slightly slower but its amplitude is markedly larger (Figure D.15.d).  
 976 The remaining solitons of the train are well located, but a secondary trough is  
 977 generated between the first two solitons whereas it is absent in **SimRef+**.

978 Using the larger mode-1 speed  $c_1$  instead of  $c^*$  (Figure D.15.b), the train  
 979 of solitons in KdV is too fast. When the eKdV equation is used with speed  $c^*$   
 980 (e), the solitons are too slow, whereas this same extended equation with  $c_1$  (c)  
 981 leads to a correct displacement of the solitons. Overall, the temporal evolution of  
 982 solitary waves in **SimRef+** is consistent with the solutions of the KdV or eKdV  
 983 equation (D.1). However, the KdV or eKdV framework remains an inviscid  
 984 simplification. Note that closer evolution of soliton amplitudes between KdV  
 985 or eKdV and **SimRef+** solutions can be obtained by simply adding a diffusive  
 986 term in KdV or eKdV equation. This also slows down propagation in KdV, and  
 987 to a lesser extent in eKdV (not shown).

988 The KdV or eKdV model also involves adjustable parameters, such as the  
 989 linear wave speed, which ranges between the interfacial speed  $c^*$  and the mode-1  
 990 speed  $c_1$ , each being one particular approximation of the wave's behaviour.

991 That being said, the wave trains in **SimRef+** are appropriately modeled as  
 992 KdV or eKdV ISWs, which confirms (i) the propagation of interfacial troughs  
 993 as trains of solitons and (ii) CROCO's ability to simulate the subtle balance  
 994 between nonhydrostatic effects (responsible for dispersion) and nonlinear ad-  
 995 vection.

---

<sup>3</sup>Due to the extension of the domain to the east, a new value of  $\rho_0$  is computed :  $\rho_0 = 1033.9 \text{ kg/m}^3$  to optimize computations.

996 *Acknowledgments.* This work was partly funded by the DGA "Etude Amont"  
 997 Protevs driven by the Shom. It was granted access to the HPC ressources of  
 998 CALMIP supercomputing center under the allocation P18017. We also grate-  
 999 fully thank the computer team of the *Laboratoire d'Arologie* for its support.  
 1000 Margaux Hilt's PhD thesis was funded by a MESRI scholarship.

## 1001 References

- 1002 Auclair, F., Bordoïs, L., Dossmann, Y., Duhaut, T., Paci, A., Ulses, C., Nguyen,  
 1003 C., 2018. A non-hydrostatic non-Boussinesq algorithm for free-surface ocean  
 1004 modelling. *Ocean Modelling* 132, 12 – 29. doi:[https://doi.org/10.1016/](https://doi.org/10.1016/j.ocemod.2018.07.011)  
 1005 [j.ocemod.2018.07.011](https://doi.org/10.1016/j.ocemod.2018.07.011).
- 1006 Bethoux, J., 1979. Budgets of the mediterranean sea. Their dependance on the  
 1007 local climate and on the characteristics of the atlantic waters. *Oceanologica*  
 1008 *Acta* 2, 157–163.
- 1009 Biscara, L., Maspataud, A., Schmitt, T., 2016. Generation of bathymetric  
 1010 digital elevation models along French coasts: Coastal risk assessment. *Hydro*  
 1011 *International* 20, 26–29.
- 1012 Borges, R., Carmona, M., Costa, B., Don, W., 2008. An improved weighted  
 1013 essentially non-oscillatory scheme for hyperbolic conservation laws. *Journal*  
 1014 *of Computational Physics* 227, 3191–3211.
- 1015 Bormans, M., Garrett, C., 1989. The effect of rotation on the surface inflow  
 1016 through the Strait of Gibraltar. *Journal of Physical Oceanography* 19, 1535–  
 1017 1542. doi:10.1175/1520-0485(1989)019<1535:TEOROT>2.0.CO;2.
- 1018 Brandt, P., Alpers, W., Backhaus, J., 1996. Study of the generation and prop-  
 1019 agation of internal waves in the Strait of Gibraltar using a numerical model  
 1020 and synthetic aperture radar images of the european ERS 1 satellite. *Journal*  
 1021 *of Geophysical Research* 101, 14237–14252. doi:10.1029/96JC00540.
- 1022 Bray, N.A., Ochoa, J., Kinder, T.H., 1995. The role of the interface in exchange  
 1023 through the Strait of Gibraltar. *Journal of Geophysical Research* 100, 10755–  
 1024 10776. doi:10.1029/95JC00381.
- 1025 Bruno, M., Alonso, J.J., Cózar, A., Viad, J., Ruiz-Cañavate, A., Echevarría, F.,  
 1026 Ruiz, J., 2002. The boiling-water phenomena at Camarinal Sill, the Strait of  
 1027 Gibraltar. *Deep-Sea Research II* 49, 4097–4113. doi:[https://doi.org/10.](https://doi.org/10.1016/S0967-0645(02)00144-3)  
 1028 [1016/S0967-0645\(02\)00144-3](https://doi.org/10.1016/S0967-0645(02)00144-3).
- 1029 Bryden, H., Candela, J., Kinder, T., 1994. Exchange through the Strait of  
 1030 Gibraltar. *Progress in Oceanography* 33, 201–248. doi:[https://doi.org/](https://doi.org/10.1016/0079-6611(94)90028-0)  
 1031 [10.1016/0079-6611\(94\)90028-0](https://doi.org/10.1016/0079-6611(94)90028-0).
- 1032 Bryden, H., Kinder, T., 1991. Steady two-layer exchange through the Strait of  
 1033 Gibraltar. *Deep Sea Research Part A. Oceanographic Research Papers* 38,  
 1034 S445–S463. doi:10.1016/S0198-0149(12)80020-3.

1035 Bryden, H., Stommel, H., 1984. Limiting processes that determine basic features  
1036 of the circulation in the Mediterranean Sea. *Oceanologica Acta* 7, 289–296.

1037 Candela, J., Winant, C., Ruiz, A., 1990. Tides in the Strait of Gibraltar.  
1038 *Journal of Geophysical Research: Oceans* 95, 7313–7335. doi:10.1029/  
1039 JC095iC05p07313.

1040 Chelton, D.B., Schlax, M.G., Samelson, R.M., de Szoeke, R.A., 2007. Global  
1041 observations of large oceanic eddies. *Geophysical Research Letters* 34. doi:10.  
1042 1029/2007GL030812.

1043 Cushman-Roisin, B., Beckers, J.M., 2011. Introduction to geophysical fluid  
1044 dynamics : physical and numerical aspects. International geophysics series  
1045 101. 2nd edition ed., Academic Press, Waltham, Mass.

1046 Debreu, L., Marchesiello, P., Penven, P., Cambon, G., 2012. Two-way nesting  
1047 in split-explicit ocean models: algorithms, implementation and validation.  
1048 *Ocean Modelling* 49–50, 1–21. doi:https://doi.org/10.1016/j.ocemod.  
1049 2012.03.003.

1050 Dossmann, Y., 2012. Ondes internes générées sur une dorsale océanique : du lab-  
1051 oratoire à l’océan. Doctoral dissertation. Université Paul Sabatier - Toulouse  
1052 III. URL: HAL. (<https://tel.archives-ouvertes.fr/tel-00758207>).

1053 Egbert, G.D., Erofeeva, S.Y., 2002. Efficient inverse modeling of barotropic  
1054 ocean tides. *Journal of Atmospheric and Oceanic Technology* 19.2, 183–204.

1055 Farmer, D., Armi, L., 1986. Maximal two-layer exchange over a sill and through  
1056 the combination of a sill and contraction with barotropic flow. *Journal of Fluid*  
1057 *Mechanics* 164, 53–76. doi:10.1017/S002211208600246X.

1058 Farmer, D., Armi, L., 1988. The flow of atlantic water through the strait of  
1059 gibraltar. *Progress in Oceanography* 21, 1–103. doi:https://doi.org/10.  
1060 1016/0079-6611(88)90055-9.

1061 Fox-Kemper, B., Adcroft, A., Böning, C.W., Chassignet, E.P., Curchitser, E.,  
1062 Danabasoglu, G., Eden, C., England, M.H., Gerdes, R., Greatbatch, R.J.,  
1063 Griffies, S.M., Hallberg, R.W., Hanert, E., Heimbach, P., Hewitt, H.T., Hill,  
1064 C.N., Komuro, Y., Legg, S., Le Sommer, J., Masina, S., Marsland, S.J.,  
1065 Penny, S.G., Qiao, F., Ringler, T.D., Treguier, A.M., Tsujino, H., Uotila, P.,  
1066 Yeager, S.G., 2019. Challenges and prospects in ocean circulation models.  
1067 *Front. Mar. Sci.* 6, 65. doi:10.3389/fmars.2019.00065.

1068 García-Lafuente, J., Sánchez-Román, A., Naranjo, C., Sánchez-Garrido, J.C.,  
1069 2011. The very first transformation of the mediterranean outflow in the strait  
1070 of gibraltar. *Journal of Geophysical Research: Oceans* 116. doi:10.1029/  
1071 2011JC006967.

1072 Garrett, C., Bormans, M., Thompson, K., 1990. The Physical Oceanography of  
1073 Sea Straits. chapter Is the exchange through the Strait of Gibraltar maximal  
1074 or submaximal ? pp. 271–294. doi:[10.1007/978-94-009-0677-8\\_13](https://doi.org/10.1007/978-94-009-0677-8_13).

1075 Gill, A.E., 1982. Atmosphere-Ocean Dynamics. International geophysics series  
1076 30, Academic Press.

1077 Grinstein, F., Margolin, L., Rider, W., 2007. Implicit Large Eddy Simulation :  
1078 Computing Turbulent Fluid Dynamics. Cambridge University Press ed.

1079 Izquierdo, A., Tejedor, L., Sein, D., Backhaus, J., Brandt, P., Rubino, A.,  
1080 Kagan, B.A., 2001. Control variability and internal bore evolution in the  
1081 Strait of Gibraltar: A 2-D two-layer model study. Estuarine, Coastal and  
1082 Shelf Science 53, 637–651. doi:<https://doi.org/10.1006/ecss.2000.0706>.

1083 Lemarié, F., Burchard, H., Debreu, L., Klingbeil, K., Sainte-Marie, J., 2019.  
1084 Advancing dynamical cores of oceanic models across all scales. Bull. Amer.  
1085 Meteor. Soc. 100, ES109–ES115. doi:[10.1175/BAMS-D-18-0303.1](https://doi.org/10.1175/BAMS-D-18-0303.1).

1086 Marchesiello, P., Capet, X., Menkes, C., Kennan, S.C., 2011. Submesoscale  
1087 dynamics in tropical instability waves. Ocean Modelling 39, 31–46.

1088 Marchesiello, P., McWilliams, J.C., Shchepetkin, A., 2001. Open boundary con-  
1089 ditions for long-term integration of regional oceanic models. Ocean modelling  
1090 3, 1–20.

1091 Millot, C., 2014. Heterogeneities of in- and out-flows in the mediterranean sea.  
1092 Progress in Oceanography 120, 254 – 278. doi:<https://doi.org/10.1016/j.pocean.2013.09.007>.

1094 Naranjo, C., Garcia-Lafuente, J., Sannino, G., Sanchez-Garrido, J., 2014. How  
1095 much do tides affect the circulation of the Mediterranean Sea? from local pro-  
1096 cesses in the Strait of Gibraltar to basin-scale effects. Progress in Oceanogra-  
1097 phy 127, 108–116. doi:<https://doi.org/10.1016/j.pocean.2014.06.005>.

1098 Naranjo, C., Sammartino, S., Garca-Lafuente, J., Bellanco, M.J., Taupier-  
1099 Letage, I., 2015. Mediterranean waters along and across the strait of gibraltar,  
1100 characterization and zonal modification. Deep Sea Research Part I: Oceano-  
1101 graphic Research Papers 105, 41 – 52. doi:<https://doi.org/10.1016/j.dsr.2015.08.003>.

1103 Pairaud, I., Auclair, F., 2005. Combined wavelet and principal component anal-  
1104 ysis (WEof) of a scale-oriented model of coastal ocean gravity waves. Dynam-  
1105 ics of atmospheres and oceans 40, 254–282. doi:[10.1016/j.dynatmoce.2005.](https://doi.org/10.1016/j.dynatmoce.2005.06.001)  
1106 06.001.

1107 Sammartino, S., García Lafuente, J., Naranjo, C., Sánchez Garrido, J., Sánchez  
1108 Leal, R., Sánchez Román, A., 2015. Ten years of marine current measurements  
1109 in Espartel Sill, Strait of Gibraltar. Journal of Geophysical Research 120,  
1110 6309–6328. doi:[10.1002/2014JC010674](https://doi.org/10.1002/2014JC010674).

1111 Sánchez Garrido, J., Lafuente, J.G., Aldeanueva, F.C., Baquerizo, A., Sannino,  
1112 G., 2008. Time-spatial variability observed in velocity of propagation of the  
1113 internal bore in the Strait of Gibraltar. *Journal of Geophysical Research* 113.  
1114 doi:10.1029/2007JC004624.

1115 Sánchez Garrido, J., Sannino, G., Liberti, L., Lafuente, J.G., Pratt, L., 2011.  
1116 Numerical modeling of three-dimensional stratified tidal flow over Camarinal  
1117 Sill, Strait of Gibraltar. *Journal of Geophysical Research* 116. doi:10.1029/  
1118 2011JC007093.

1119 Sannino, G., Bargagli, A., Artale, V., 2002. Numerical modeling of the mean  
1120 excgchange through the Strait of Gibraltar. *Journal of Geophysical Research*  
1121 107. doi:10.1029/2001JC000929.

1122 Sannino, G., Bargagli, A., Artale, V., 2004. Numerical modeling of the semidi-  
1123 urnal tidal exchange through the Strait of Gibraltar. *Journal of Geophysical*  
1124 *Research* 109. doi:10.1029/2003JC002057.

1125 Sannino, G., Garrido, J.S., Liberti, L., Pratt, L., 2014. Exchange flow through  
1126 the Strait of Gibraltar as simulated by a  $\sigma$ -Coordinate Hydrostatic Model and  
1127 a z-coordinate nonhydrostatic model. *American Geophysical Union (AGU)*.  
1128 chapter 3. pp. 25–50. doi:10.1002/9781118847572.ch3.

1129 Sannino, G., Herrmann, M., Carillo, A., Rupolo, V., Ruggiero, V., Artale, V.,  
1130 Heimbach, P., 2009a. An eddy-permitting model of the Mediterranean Sea  
1131 with two-way grid refinement at the Strait of Gibraltar. *Ocean Modelling* 30,  
1132 56–72. doi:https://doi.org/10.1016/j.ocemod.2009.06.002.

1133 Sannino, G., Pratt, L., Carillo, A., 2009b. Hydraulic criticality of the exchange  
1134 flow through the Strait of Gibraltar. *Journal of Physical Oceanography* 39,  
1135 2779–2799. doi:https://doi.org/10.1175/2009JP04075.1.

1136 Shchepetkin, A., McWilliams, J., 2005. The regional oceanic modeling sys-  
1137 tem (ROMS): a split-explicit, free-surface, topography-following-coordinate  
1138 oceanic model. *Ocean Modelling* 9, 347–404. doi:https://doi.org/10.1016/  
1139 j.ocemod.2004.08.002.

1140 Soto-Navarro, J., Somot, S., Sevault, F., Beuvier, J., Criado-Aldeanueva, F.,  
1141 García-Lafuente, J., Branger, K., 2015. Evaluation of regional ocean circula-  
1142 tion models for the Mediterranean Sea at the Strait of Gibraltar: volume  
1143 transport and thermohaline properties of the outflow. *Climate Dynamics* 44,  
1144 1277–1292. doi:10.1007/s00382-014-2179-4.

1145 Soufflet, Y., Marchesiello, P., Lemarié, F., Jouanno, J., Capet, X., Debreu, L.,  
1146 Benshila, R., 2016. On effective resolution in ocean models. *Ocean Modelling*  
1147 98, 36–50.

1148 St. Laurent, L., Garrett, C., 2002. The role of internal tides in mixing the  
1149 deep ocean. *Journal of Physical Oceanography* 32, 2882–2899. doi:10.1175/  
1150 1520-0485(2002)032<2882:TROI>2.0.CO;2.

- 1151 Vallis, G., 2006. Atmospheric and Oceanic Fluid Dynamics : fundamentals and  
1152 large-scale circulation. Cambridge University Press ed.
- 1153 Vázquez, A., Stashchuk, N., Vlasenko, V., Bruno, M., Izquierdo, A., Gal-  
1154 lacher, P.C., 2006. Evidence of multimodal structure of the baroclinic tide  
1155 in the Strait of Gibraltar. Geophysical research letters 33. doi:10.1029/  
1156 2006GL026806.
- 1157 Vlasenko, V., Garrido, J.S., Stashchuk, N., Lafuente, J.G., Losada, M., 2009.  
1158 Three-dimensional evolution of large-amplitude internal waves in the Strait  
1159 of Gibraltar. Journal of physical oceanography 39, 2230–2246. doi:https:  
1160 //doi.org/10.1175/2009JP04007.1.
- 1161 Wesson, J., Gregg, M., 1994. Mixing at Camarinal Sill in the Strait of Gibralt-  
1162 ar. Journal of Geophysical Research: Oceans 99, 9847–9878. doi:10.1029/  
1163 94JC00256.

## 1164 List of Figures

1165	D.1	Illustration of small-scale processes in the Strait of Gibraltar induced by tidal interaction with stratification and bathymetry. (a)	
1166		Linear / Small amplitude internal wave. (b) Hydraulic Jump.	
1167		(c) Kelvin-Helmholtz instabilities. (d) Large-amplitude internal	
1168		waves or internal solitary waves (ISW). . . . .	35
1169	D.2	a) Bathymetry of the strait of Gibraltar, with the section used	
1170		for the present model configuration (white dotted line). Black	
1171		squares indicate the position of moorings from Candela et al.	
1172		(1990); ES: Espartel Sill, TB: Tanger Basin, CS: Camarinal Sill	
1173		, TN: Tarifa Narrows. b) Width of the Gibraltar Strait along	
1174		transverse direction (y) between 2 isobaths of depth h. . . . .	36
1175	D.3	Initial salinity (solid) and temperature (dashed) profiles of Mediter-	
1176		anean water (black) and Atlantic water (grey). . . . .	37
1177	D.4	a - b ) Longitudinal currents $u$ (greyscale) and isopycnals (thin	
1178		black lines) of density anomaly between $-2 \text{ kg m}^{-3}$ and $0.5 \text{ kg}$	
1179		$\text{m}^{-3}$ with an interval of $0.5 \text{ kg m}^{-3}$ at $t = 72 \text{ h}$ at the end of	
1180		the spin-up phase for <b>SimAllCor</b> (a) and <b>SimNoCor</b> (b). The	
1181		bold line is for isopycnal $\rho' = -0.7 \text{ kg/m}^3$ . The vertical dashed	
1182		lines indicate the location of the profiles given in c and d. Color	
1183		contours in (a) indicate the values of transverse currents $v$ . Inside	
1184		the red contours $v \geq 0.5 \text{ m/s}$ , while inside the blue contours	
1185		$v \leq -0.5 \text{ m/s}$ . c - d ) 3T-averaged longitudinal currents (black)	
1186		and transverse currents (grey) for <b>SimRef</b> (plain), <b>SimAllCor</b>	
1187		(dashed) and <b>SimNoCor</b> (dotted). Observation of tidal-mean	
1188		currents at stations M2 and M7 (Fig. D.2) from Candela et al.	
1189		(1990) (squares). . . . .	38
1190	D.5	Isopycnal position averaged over a 3T time interval in <b>SimRef</b>	
1191		(thin black lines are density anomaly contours between $-1.5 \text{ kg}$	
1192		$\text{m}^{-3}$ and $0.5 \text{ kg m}^{-3}$ with an interval of $0.5 \text{ kg m}^{-3}$ ; Thick black	
1193		(grey) contours indicate critical Froud number $F = 1$ during flood	
1194		(ebb) tide, inside which the flow is supercritical. . . . .	39
1195	D.6	a) Density anomaly (greyscale ; $\text{kg/m}^3$ ) in the lee side of Ca-	
1196		marinal Sill in <b>SimRef</b> at $t = 7.56 \text{ T}$ . Black contours indicate	
1197		the location where the Richardson number is 0.25. b) Vertical	
1198		velocity (greyscale ; $\text{m/s}$ ) in the lee side of Camarinal Sill in	
1199		<b>SimRef</b> at $t = 7.56 \text{ T}$ . The black contour indicates the location	
1200		where the Froude number is 1. a) and b) The black and white	
1201		contour represents $OW = -4 * 10^{-4} \text{ s}^{-2}$ . . . . .	40
1202			

1203	D.7	a) Mean field of longitudinal velocity $u$ (m/s) ; greyscale) and	
1204		isopycnals (black lines, density anomaly between $-1.6 \text{ kg m}^{-3}$	
1205		and $0.5 \text{ kg m}^{-3}$ with an interval of $0.3 \text{ kg m}^{-3}$ ) with location	
1206		of $Ri < 0.25$ (white dots). b) Vertical velocity $w$ (greyscale ; m/s)	
1207		and velocity vectors of the superposition of the second and third	
1208		singular vectors of the SVD decomposition added to the mean	
1209		velocity field of (a). Black and white contours are $OW = -1.5 * 10^{-4} \text{ s}^{-2}$	41
1210			
1211	D.8	Density anomaly fields ( $\rho$ ; $\text{kg/m}^3$ ) of <b>SimRef</b> zoomed over CS at	
1212		$t = 7.7 \text{ T}$ (a) and $t = 7.9 \text{ T}$ (b). The position of $\rho' = -0.7 \text{ kg/m}^3$	
1213		isopycnal is shown in white. c) Profiles of vertical velocity at the	
1214		position marked by a triangle in (a)-black and (b)-grey. . . . .	42
1215	D.9	(a) Depth-averaged currents over CS. (b) Space-time diagram	
1216		of the vertical displacement of isopycnal $\rho' = -0.7 \text{ kg/m}^3$ of	
1217		<b>SimRef</b> ( $\Delta z = 50 \text{ m}$ between two contours). The black line	
1218		indicates the time used in the bottom panel. (c) vertical velocity	
1219		field (greyscale) and isopycnals (black lines ; density anomaly	
1220		between $-1.9 \text{ kg m}^{-3}$ and $0.5 \text{ kg m}^{-3}$ with an interval of $0.3 \text{ kg m}^{-3}$ )	
1221		at the time indicated in panel (b). In white is the isopycnal	
1222		$\rho' = -0.7 \text{ kg/m}^3$ . . . . .	43
1223	D.10	Comparison of experiments <b>SimS</b> and <b>SimRef</b> showing the ef-	
1224		fect of tidal amplitude on the generation of solitary waves. a)	
1225		Relative density ( $\text{kg/m}^3$ ) in <b>SimS</b> during a hydraulic jump ( $t =$	
1226		$7.5 \text{ T}$ ) at Camarinal Sill. Regions where $F > 1$ are indicated for	
1227		both <b>SimS</b> (bold lines) and <b>SimRef</b> (dashed lines). New features	
1228		appear with stronger tides: a mode-1 disturbance "a" trapped up-	
1229		stream of the CS; an additional supercritical area ( $F > 1$ ) noted	
1230		"b" in the bottom layer of a secondary relief. b) Relative density	
1231		in <b>SimS</b> (greyscale) and <b>SimRef</b> (dashed lines) at $t = 8.5 \text{ T}$ ,	
1232		showing the tidal amplitude effect on eastward propagating soli-	
1233		tary waves generated at CS. . . . .	44
1234	D.11	Vertical velocity (greyscale ; $\text{m/s}$ ) and isopycnals (black lines ;	
1235		density anomaly between $-1.5 \text{ kg m}^{-3}$ and $0.5 \text{ kg m}^{-3}$ with an	
1236		interval of $0.5 \text{ kg m}^{-3}$ ) in <b>SimLH</b> . . . . .	45
1237	D.12	Internal wave propagation from density field at $t = 8.1 \text{ T}$ in (a)	
1238		<b>SimRef</b> ; (b) <b>SimW</b> ; (c) <b>SimH</b> ; (d) <b>SimV</b> ; (e) <b>SimL</b> ; and (f)	
1239		<b>SimLH</b> . Large amplitude mode-1 waves (soliton or bore) are	
1240		denoted as "1" and mode 2 as "2". . . . .	46
1241	D.13	a) $N$ frequency computed at $5.8^\circ \text{W}$ longitude and time-averaged	
1242		between $8.2 \text{ T}$ and $8.7 \text{ T}$ (during flood tide and presence of hy-	
1243		draulic jump). b) Same as (a) but at $5.55^\circ \text{W}$ longitude. . . . .	47
1244	D.14	a) Field of longitudinal velocity ( $u(x, z)$ ) at $t = 8.5 \text{ T}$ with con-	
1245		tours of mode-1 supercritical region ( $F > 1$ ) calculated from a 3T-	
1246		averaged stratification. b) Computed speed of mode-1 linear in-	
1247		ternal waves ( $c_1(x)$ ) from a 3T-averaged stratification in config-	
1248		uration <b>SimRef</b> . . . . .	48

1249	D.15 a) Isopycnal $\rho' = -0.2 \text{ kg/m}^3$ simulated by CROCO in <b>SimRef+</b>	
1250	at $t = 7.5 T$ (grey line; the interface depth is left constant	
1251	downstream of the wave) and at $t = 7.75 T$ (black line). b-e)	
1252	Evolution of the interface simulated by KdV or eKdV (bold) and	
1253	<b>SimRef+</b> (solid line) at $t = 7.75 T$ . Two propagation speeds	
1254	are used: $c^*$ (d,e) and $c_1$ (b,c) (see text for details). . . . .	49

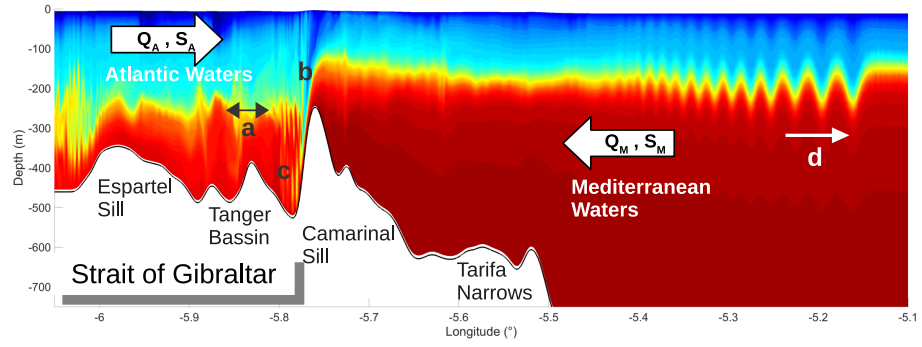


Figure D.1: Illustration of small-scale processes in the Strait of Gibraltar induced by tidal interaction with stratification and bathymetry. (a) Linear / Small amplitude internal wave. (b) Hydraulic Jump. (c) Kelvin-Helmholtz instabilities. (d) Large-amplitude internal waves or internal solitary waves (ISW).

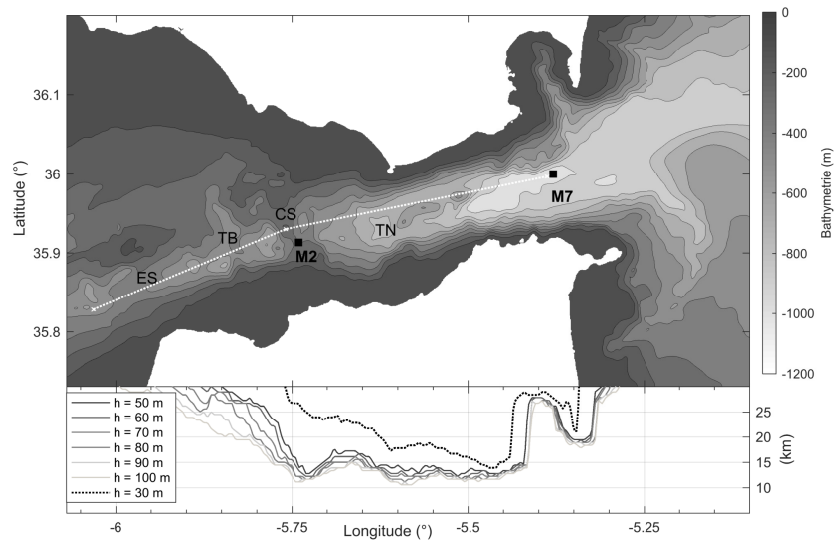


Figure D.2: a) Bathymetry of the strait of Gibraltar, with the section used for the present model configuration (white dotted line). Black squares indicate the position of moorings from Candela et al. (1990); ES: Espartel Sill, TB: Tanger Basin, CS: Camarinal Sill, TN: Tarifa Narrows. b) Width of the Gibraltar Strait along transverse direction (y) between 2 isobaths of depth  $h$ .

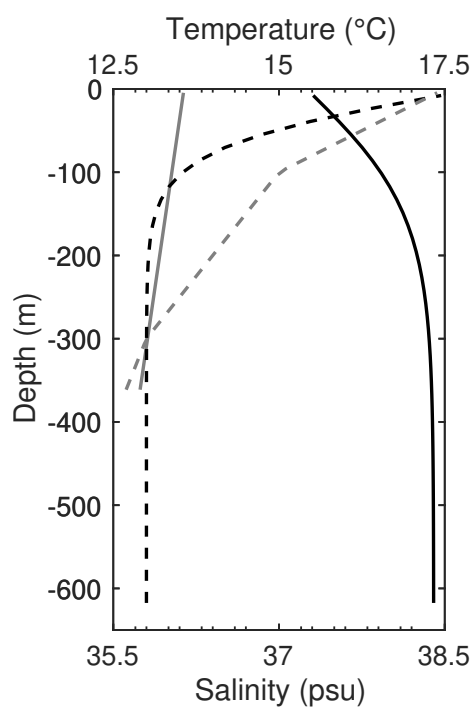


Figure D.3: Initial salinity (solid) and temperature (dashed) profiles of Mediterranean water (black) and Atlantic water (grey).

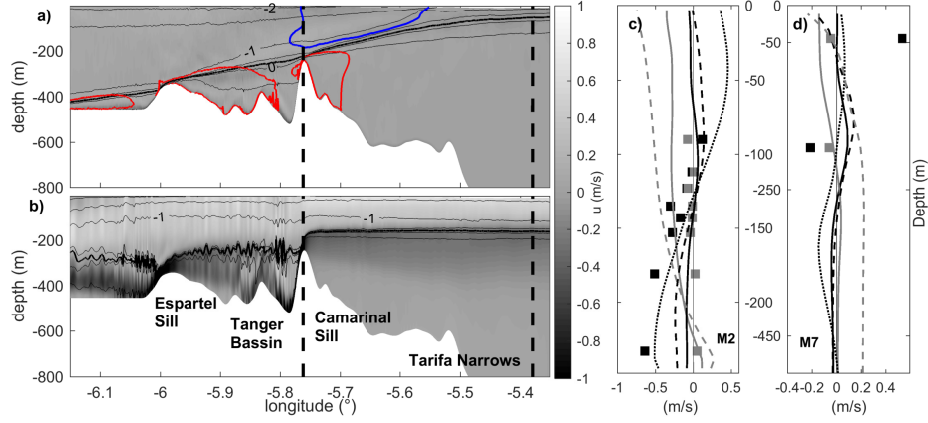


Figure D.4: a - b ) Longitudinal currents  $u$  (greyscale) and isopycnals (thin black lines) of density anomaly between  $-2 \text{ kg m}^{-3}$  and  $0.5 \text{ kg m}^{-3}$  with an interval of  $0.5 \text{ kg m}^{-3}$  at  $t = 72 \text{ h}$  at the end of the spin-up phase for **SimAllCor** (a) and **SimNoCor** (b). The bold line is for isopycnal  $\rho' = -0.7 \text{ kg/m}^3$ . The vertical dashed lines indicate the location of the profiles given in c and d. Color contours in (a) indicate the values of transverse currents  $v$ . Inside the red contours  $v \geq 0.5 \text{ m/s}$ , while inside the blue contours  $v \leq -0.5 \text{ m/s}$ . c - d ) 3T-averaged longitudinal currents (black) and transverse currents (grey) for **SimRef** (plain), **SimAllCor** (dashed) and **SimNoCor** (dotted). Observation of tidal-mean currents at stations M2 and M7 (Fig. D.2) from Candela et al. (1990) (squares).

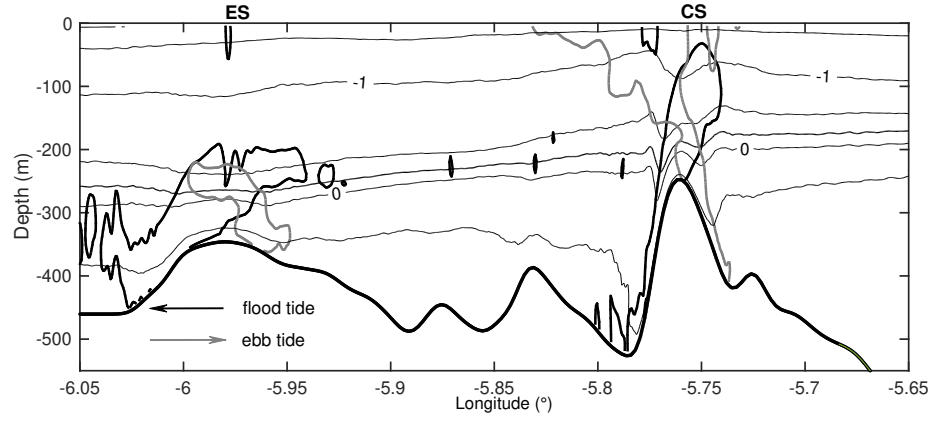


Figure D.5: Isopycnal position averaged over a  $3T$  time interval in **SimRef** (thin black lines are density anomaly contours between  $-1.5 \text{ kg m}^{-3}$  and  $0.5 \text{ kg m}^{-3}$  with an interval of  $0.5 \text{ kg m}^{-3}$ ; Thick black (grey) contours indicate critical Froude number  $F = 1$  during flood (ebb) tide, inside which the flow is supercritical).

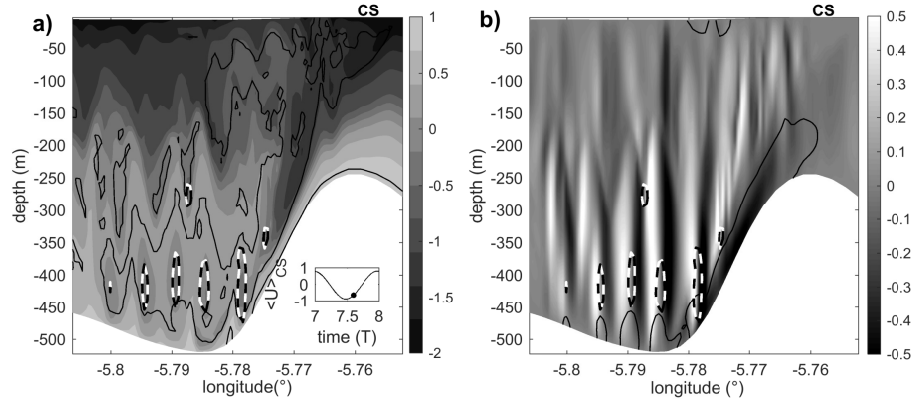


Figure D.6: a) Density anomaly (greyscale ;  $kg/m^3$ ) in the lee side of Camarinal Sill in **SimRef** at  $t = 7.56$  T. Black contours indicate the location where the Richardson number is 0.25. b) Vertical velocity (greyscale ;  $m/s$ ) in the lee side of Camarinal Sill in **SimRef** at  $t = 7.56$  T. The black contour indicates the location where the Froude number is 1. a) and b) The black and white contour represents  $OW = -4 * 10^{-4} s^{-2}$ .

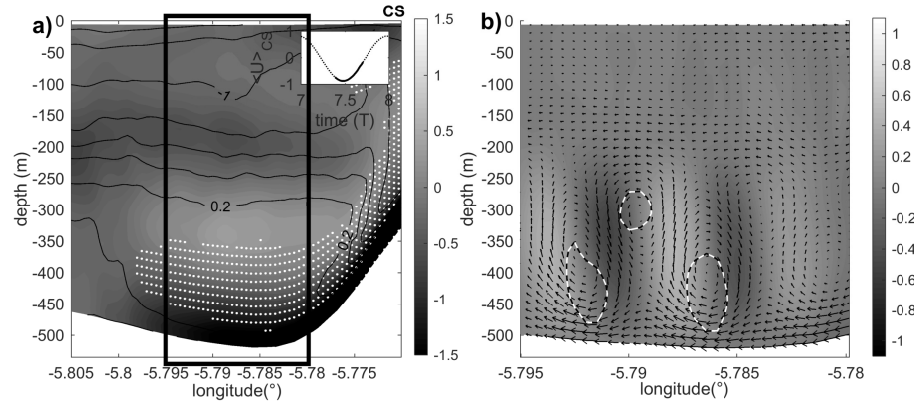


Figure D.7: a) Mean field of longitudinal velocity  $u$  (m/s ; greyscale) and isopycnals (black lines, density anomaly between  $-1.6 \text{ kg m}^{-3}$  and  $0.5 \text{ kg m}^{-3}$  with an interval of  $0.3 \text{ kg m}^{-3}$ ) with location of  $Ri < 0.25$  (white dots). b) Vertical velocity  $w$  (greyscale ; m/s) and velocity vectors of the superposition of the second and third singular vectors of the SVD decomposition added to the mean velocity field of (a). Black and white contours are  $OW = -1.5 \times 10^{-4} \text{ s}^{-2}$

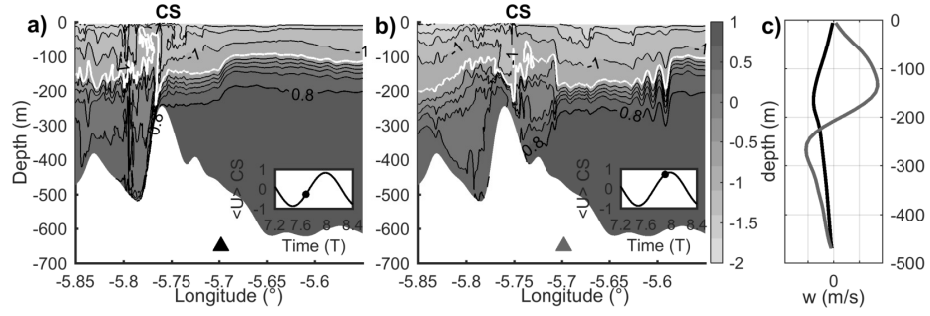


Figure D.8: Density anomaly fields ( $\rho'$  ;  $kg/m^3$ ) of **SimRef** zoomed over CS at  $t = 7.7$  T (a) and  $t = 7.9$  T (b). The position of  $\rho' = -0.7$   $kg/m^3$  isopycnal is shown in white. c) Profiles of vertical velocity at the position marked by a triangle in (a)-black and (b)-grey.

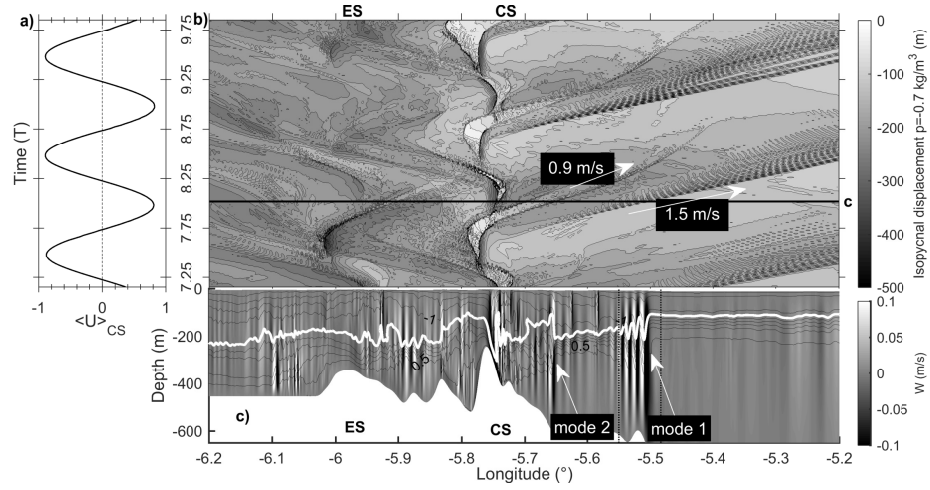


Figure D.9: (a) Depth-averaged currents over CS. (b) Space-time diagram of the vertical displacement of isopycnal  $\rho' = -0.7 \text{ kg/m}^3$  of **SimRef** ( $\Delta z = 50 \text{ m}$  between two contours). The black line indicates the time used in the bottom panel. (c) vertical velocity field (greyscale) and isopycnals (black lines ; density anomaly between  $-1.9 \text{ kg m}^{-3}$  and  $0.5 \text{ kg m}^{-3}$  with an interval of  $0.3 \text{ kg m}^{-3}$  ) at the time indicated in panel (b). In white is the isopycnal  $\rho' = -0.7 \text{ kg/m}^3$ .

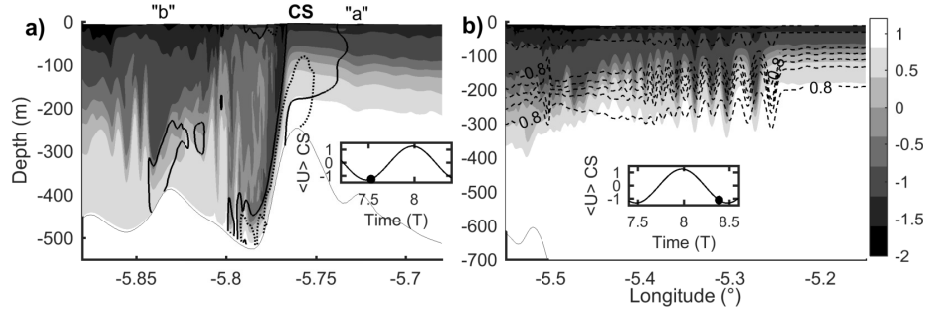


Figure D.10: Comparison of experiments **SimS** and **SimRef** showing the effect of tidal amplitude on the generation of solitary waves. a) Relative density ( $kg/m^3$ ) in **SimS** during a hydraulic jump ( $t = 7.5 T$ ) at Camarinal Sill. Regions where  $F > 1$  are indicated for both **SimS** (bold lines) and **SimRef** (dashed lines). New features appear with stronger tides: a mode-1 disturbance "a" trapped upstream of the CS; an additional supercritical area ( $F > 1$ ) noted "b" in the bottom layer of a secondary relief. b) Relative density in **SimS** (greyscale) and **SimRef** (dashed lines) at  $t = 8.5 T$ , showing the tidal amplitude effect on eastward propagating solitary waves generated at CS.

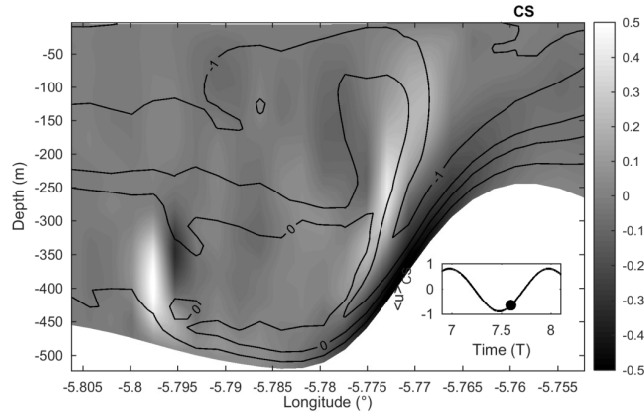


Figure D.11: Vertical velocity (greyscale ;  $m/s$  ) and isopycnals (black lines ; density anomaly between  $-1.5 \text{ kg m}^{-3}$  and  $0.5 \text{ kg m}^{-3}$  with an interval of  $0.5 \text{ kg m}^{-3}$  ) in **SimLH**.

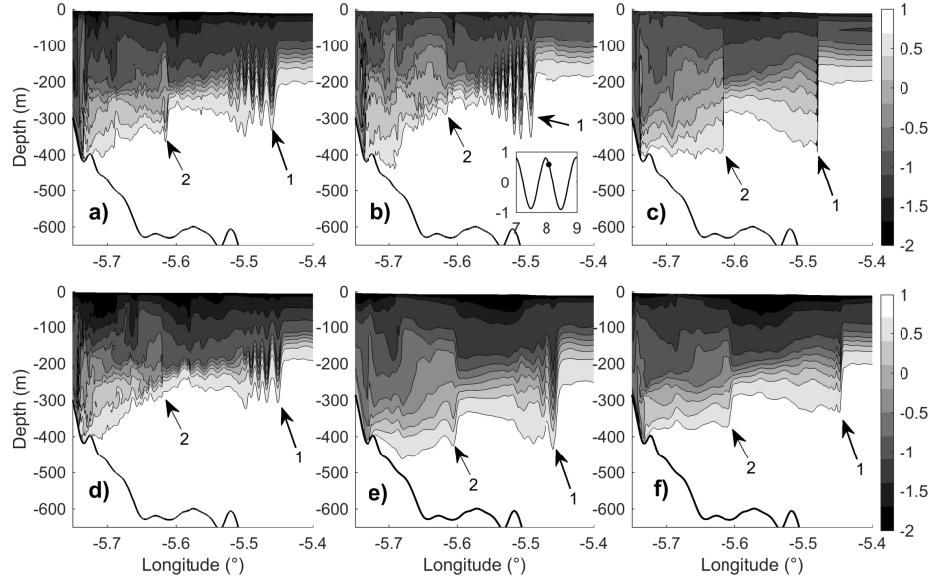


Figure D.12: Internal wave propagation from density field at  $t = 8.1T$  in (a) **SimRef**; (b) **SimW**; (c) **SimH**; (d) **SimV**; (e) **SimL**; and (f) **SimLH**. Large amplitude mode-1 waves (soliton or bore) are denoted as "1" and mode 2 as "2".

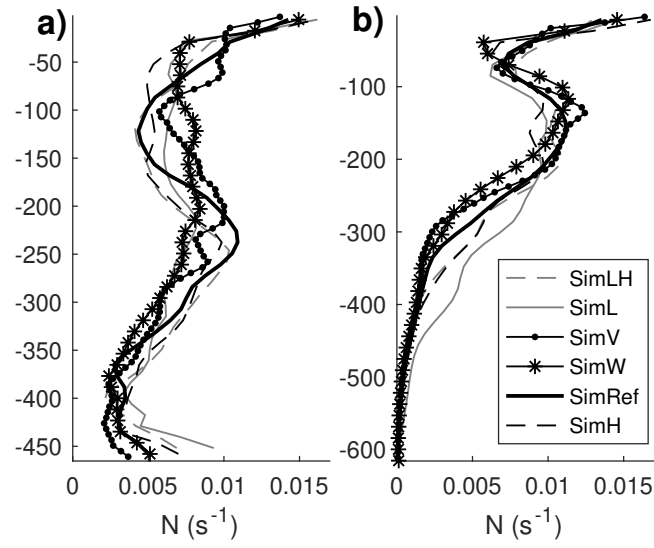


Figure D.13: a)  $N$  frequency computed at  $5.8^\circ\text{W}$  longitude and time-averaged between 8.2 T and 8.7 T (during flood tide and presence of hydraulic jump). b) Same as (a) but at  $5.55^\circ\text{W}$  longitude.

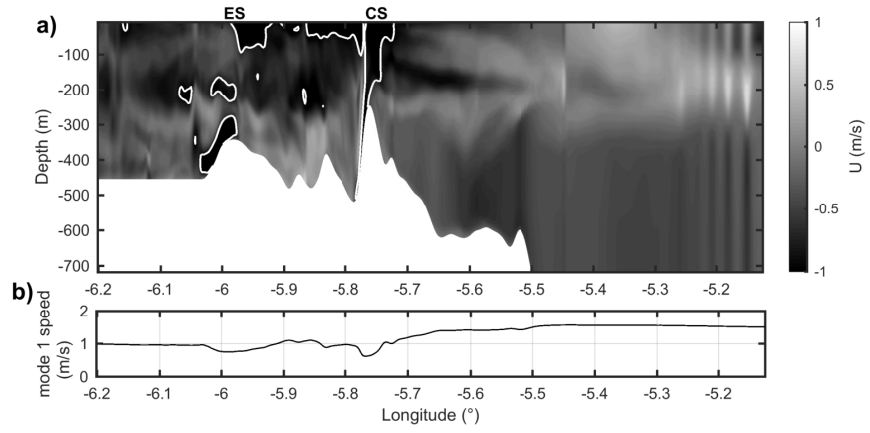


Figure D.14: a) Field of longitudinal velocity ( $u(x, z)$ ) at  $t = 8.5 T$  with contours of mode-1 supercritical region ( $F > 1$ ) calculated from a 3T-averaged stratification. b) Computed speed of mode-1 linear internal waves ( $c_1(x)$ ) from a 3T-averaged stratification in configuration **SimRef**.

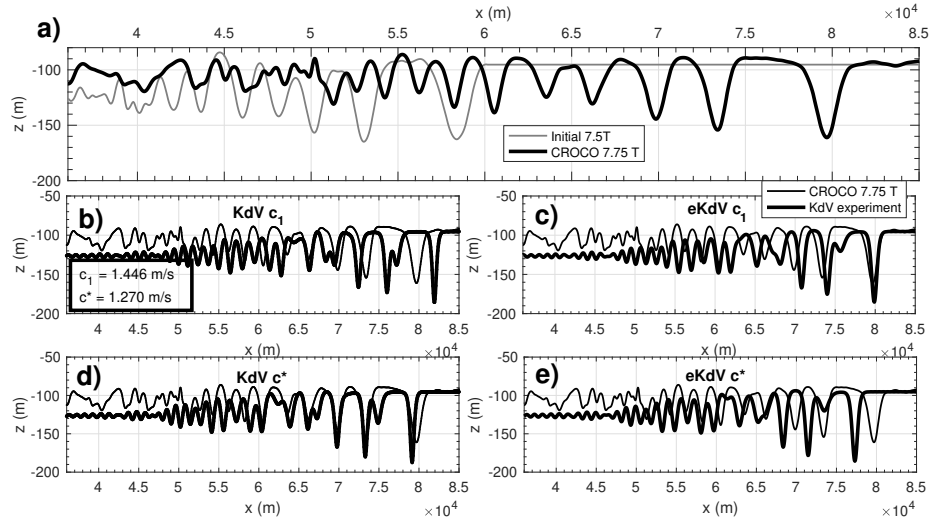


Figure D.15: a) Isopycnal  $\rho' = -0.2 \text{ kg/m}^3$  simulated by CROCO in **SimRef+** at  $t = 7.5 T$  (grey line; the interface depth is left constant downstream of the wave) and at  $t = 7.75 T$  (black line). b-e) Evolution of the interface simulated by KdV or eKdV (bold) and **SimRef+** (solid line) at  $t = 7.75 T$ . Two propagation speeds are used:  $c^*$  (d,e) and  $c_1$  (b,c) (see text for details).

1255	<b>List of Tables</b>	
1256	D.1 Numerical parameters of simulation <b>SimRef</b> . . . . .	51
1257	D.2 3T time-averaged transports ( $\text{m}^2/\text{s}$ ) at CS, depth (m) and slope	
1258	of the interface. . . . .	52
1259	D.3 Parameters of numerical sensitivity experiments. If not explicitly	
1260	indicated, $t_s$ and $t_f$ are the same as in Table D.1. . . . .	53

Table D.1: Numerical parameters of simulation **SimRef**

Number of horizontal points	2661x3	
Horizontal scale ( $\Delta x$ )	50 m	
Number of vertical $\sigma$ -levels	40	
Depth	Min	Max
	247 m	900 m
Vertical scale ( $\Delta z$ )	6 m	23 m
Slow time step ( $t_s$ )	1 s	
Fast time step ( $t_f$ )	1/8 s	
Spin up period	72 h	
Vertical Viscosity	$10^{-6}$ m <sup>2</sup> /s	
Lateral Viscosity	$10^{-5}$ m <sup>2</sup> /s	
Diffusivity	$10^{-6}$ m <sup>2</sup> /s	
Momentum Advective Scheme	TVD - Van Leer	
Turbulent Closure Scheme	none	
T, S Advective Scheme	WENO5	
Quadratic bottom drag coefficient	$10^{-3}$	
Atmospheric forcing/fluxes	none	

Table D.2: 3T time-averaged transports ( $\text{m}^2/\text{s}$ ) at CS, depth (m) and slope of the interface.

	Transport ( $\text{m}^2/\text{s}$ )		Pycnocline Depth (m)			Pycnocline Slope	
	Upper layer	Lower layer	ES ( $5.91^\circ\text{W}$ )	CS ( $5.71^\circ\text{W}$ )	TN ( $5.52^\circ\text{W}$ )	ES-CS	CS-TN
Farmer and Armi (1988)	/	/	190	125	60	0.003	0.003
<b>SimAllCor</b>	-5	-13	300	175	70	0.006	0.006
<b>SimNoCor</b>	50	-45	290	200	220	0.005	-0.001
<b>SimRef</b>	0.7	-6	245	175	160	0.004	0.001

Table D.3: Parameters of numerical sensitivity experiments. If not explicitly indicated,  $t_s$  and  $t_f$  are the same as in Table D.1.

<b>SimH</b>	Hydrostatic equations ( $t_s = 0.5s$ $t_f = 0.25s$ )
<b>SimW</b>	WENO5-Z momentum advection scheme
<b>SimV</b>	80 $\sigma$ -levels
<b>SimL</b>	220-m horizontal resolution ( $t_s = 4s$ $t_f = 0.5s$ )
<b>SimLH</b>	220-m horizontal resolution with hydrostatic equations ( $t_s = 2s$ $t_f = 1s$ )